



**HAL**  
open science

# Through analysis of the microstructure changes during linear friction welding of the near- $\alpha$ titanium alloy Ti-6Al-2Sn-4Zr-2Mo (Ti6242) towards microstructure optimization

Dorick Ballat-Durand, Salima Bouvier, Marion Risbet, Wolfgang Pantleon

## ► To cite this version:

Dorick Ballat-Durand, Salima Bouvier, Marion Risbet, Wolfgang Pantleon. Through analysis of the microstructure changes during linear friction welding of the near- $\alpha$  titanium alloy Ti-6Al-2Sn-4Zr-2Mo (Ti6242) towards microstructure optimization. *Materials Characterization*, 2019, 151, pp.38-52. 10.1016/j.matchar.2019.02.027 . hal-02889613

**HAL Id: hal-02889613**

**<https://hal.science/hal-02889613>**

Submitted on 22 Oct 2021

**HAL** is a multi-disciplinary open access archive for the deposit and dissemination of scientific research documents, whether they are published or not. The documents may come from teaching and research institutions in France or abroad, or from public or private research centers.

L'archive ouverte pluridisciplinaire **HAL**, est destinée au dépôt et à la diffusion de documents scientifiques de niveau recherche, publiés ou non, émanant des établissements d'enseignement et de recherche français ou étrangers, des laboratoires publics ou privés.



Distributed under a Creative Commons Attribution - NonCommercial 4.0 International License

Through Analysis of the Microstructure Changes During Linear Friction Welding of the  
Near- $\alpha$  Titanium Alloy Ti-6Al-2Sn-4Zr-2Mo (Ti6242) Towards Microstructure  
Optimization.

Dorick BALLAT-DURAND<sup>1</sup>, Salima BOUVIER<sup>1</sup>, Marion RISBET<sup>1</sup> and Wolfgang  
PANTLEON<sup>2</sup>

<sup>1</sup>Sorbonne Universités, Université de Technologie de Compiègne, Laboratoire Roberval  
de Mécanique, UMR-CNRS 7337, CS 60319 Rue Roger Coultolenc 60203 Compiègne  
cedex France

<sup>2</sup>Technical University of Denmark, Department of Mechanical Engineering, Section of  
Materials and Surface Engineering, Produktionstorvet 425, 2800 Kgs. Lyngby,  
Denmark

Corresponding author: dorick.ballat-durand@utc.fr, Tel. 00 33 3 44 23 40 51,  
salima.bouvier@utc.fr, marion.risbet@utc.fr, pawo@dtu.dk

Declarations of interest: none

## ABSTRACT

Linear Friction Welding (LFW) is a solid-state joining process producing narrow joints mainly developed for the aircraft industry. The thermo-mechanical loads involved in LFW lead to **significant local microstructural changes**. This study aimed at identifying the mechanisms impacting these changes in order to develop a Post-Weld Heat Treatment (PHWT) optimizing the joint microstructure. The temperature fields showed that a zone of 1 mm on either side of the weld center line experienced thermo-mechanical processing in the  $\beta$ -domain for 2 s followed by a rapid cooling to 400 °C. Inspection of the weld by

Optical Microscopy (OM) and Scanning Electron Microscopy (SEM) revealed a strongly affected microstructure characterized by a sharp microstructural refinement and the presence of defects at the interface. The joint consists of: 1) the Welding Line (WL) which underwent a complete  $\alpha \rightarrow \beta$  transformation accompanied by the recrystallization of the prior- $\beta$  grain and the development of a  $\{110\}\langle 111 \rangle$  texture followed by intragranular precipitation of textured  $\alpha'$  Hexagonal Close-Packed (HCP) martensitic laths; 2) the Thermo-Mechanically Affected Zone (TMAZ) characterized by a partial  $\alpha \rightarrow \beta$  transformation resulting in a microstructure refinement by  $\alpha$  variant selection upon cooling. A third zone, the Heat Affected Zone (HAZ), was revealed as having a microstructure indistinguishable from the base material (BM) but being slightly harder. The texture analysis of the reconstructed  $\beta$  phase in the joint core showed that the local deformation conditions were asymmetrical between the forging and the oscillating part and that the WL may have experienced a complex material stirring with turbulent flow. These microstructural changes generate an increase in hardness in the joint with a maximum increase of HV0.3 by 40% in the WL. The PWHT consisting of an  $\alpha + \beta$  annealing followed by ageing resulted in an  $\alpha' \rightarrow \alpha + \beta$  decomposition and  $\alpha$  globularization in the TMAZ leading to a gradual microstructure refinement from the BM to the WL. A rather homogenous hardness was obtained across the assembly after the PWHT.

**Key words:** Linear Friction Welding, titanium, texture, EBSD, microstructure,  $\beta$  reconstruction, recrystallization.

## ABSTRACT

Linear Friction Welding (LFW) is a solid-state joining process producing narrow joints mainly developed for the aircraft industry. The thermo-mechanical loads involved in LFW lead to significant local microstructural changes. This study aimed at identifying the mechanisms impacting these changes in order to develop a Post-Weld Heat Treatment (PWHT) optimizing the joint microstructure. The temperature fields showed that a zone of 1 mm on either side of the weld center line experienced thermo-mechanical processing in the  $\beta$ -domain for 2 s followed by a rapid cooling to 400 °C. Inspection of the weld by Optical Microscopy (OM) and Scanning Electron Microscopy (SEM) revealed a strongly affected microstructure characterized by a sharp microstructural refinement and the presence of defects at the interface. The joint consists of: 1) the Welding Line (WL) which underwent a complete  $\alpha \rightarrow \beta$  transformation accompanied by the recrystallization of the prior- $\beta$  grain and the development of a  $\{110\}\langle 111 \rangle$  texture followed by intragranular precipitation of textured  $\alpha'$  Hexagonal Close-Packed (HCP) martensitic laths; 2) the Thermo-Mechanically Affected Zone (TMAZ) characterized by a partial  $\alpha \rightarrow \beta$  transformation resulting in a microstructure refinement by  $\alpha$  variant selection upon cooling. A third zone, the Heat Affected Zone (HAZ), was revealed as having a microstructure indistinguishable from the base material (BM) but being slightly harder. The texture analysis of the reconstructed  $\beta$  phase in the joint core showed that the local deformation conditions were asymmetrical between the forging and the oscillating part and that the WL may have experienced a complex material stirring with turbulent flow. These microstructural changes generate an increase in hardness in the joint with a maximum increase of HV0.3 by 40% in the WL. The PWHT consisting of an  $\alpha + \beta$  annealing

followed by ageing resulted in an  $\alpha' \rightarrow \alpha + \beta$  decomposition and  $\alpha$  globularization in the TMAZ leading to a gradual microstructure refinement from the BM to the WL. A rather homogenous hardness was obtained across the assembly after the PWHT.

**Key words:** Linear Friction Welding, titanium, texture, EBSD, microstructure,  $\beta$  reconstruction, recrystallization.

## 1. INTRODUCTION

Near- $\alpha$  Ti-alloys such as the Ti-6Al-2Sn-4Zr-2Mo (Ti6242) are of interest for gas turbine components as they offer an advantageous compromise between tensile strength, creep resistance and toughness [1], [2].

The near- $\alpha$  alloys are known to have a fairly good weldability using conventional fusion welding techniques. Nevertheless the weld pool generated by those processes could lead to solidification defects and/or oxygen and nitrogen pollution into the joint if the protective environment is deficient [3], [4]. This pollution could be responsible for a substantial embrittlement of the weld [5], [6]. As a result, solid-state joining processes are considered as encouraging alternative techniques for joining Ti-alloys because they prevent the joint from solidification defects and environment/surface pollution [7]. Ti-alloys are excellent candidates for Linear Friction Welding (LFW) as the local friction heating in combination with their low thermal conductivity leads to the formation of thin, sound welds.

Preliminary studies on LFW Ti-alloys focused on determining indicators based on the main process parameters (amplitude, frequency, axial pressure and axial shortening) to define whether a sound joint was achieved [8], [9]. Following studies aimed at providing microstructure and mechanical characterizations of LFW joints mainly

focused on  $\alpha+\beta$  Ti-6Al-4V (Ti64) assemblies, however only few papers were dedicated to joining near- $\alpha$  alloys such as Ti6242 or IMI834 [10]–[13]. The approaches adopted in the previous studies for characterizing the microstructures relied on basic observations as their main scope was mechanical characterization. In fact, the microstructures formed in the joint appeared quite similar between  $\alpha+\beta$  and near- $\alpha$  LFW assemblies [14], [15]: highly textured ultra-fine martensitic  $\alpha'$  laths precipitating within recrystallized-like prior- $\beta$  grains in the core of the joint (100  $\mu\text{m}$  in width) with squeezed  $\alpha+\beta$  layers on the sides (1 mm in width). Such a microstructure led to a substantial hardening of the joint resulting in failure in the base material (i.e. far from the weld) upon tensile testing. As a result the authors developed PWHTs mainly for stress relieving purposes using intermediate temperature ranges (600-700  $^{\circ}\text{C}$ ) [11], [13]. However, reshaping the microstructures resulting from LFW by means of high temperature PWHTs might be of interest as the as-welded microstructures in the joint core are in a metastable state due to the displacive transformation leading to discontinuous mechanical properties across the assembly.

The present study follows on from previous investigations on LFW of the  $\beta$ -metastable Ti17 [16] aiming at: 1) characterizing the very local microstructures and crystallographic configurations; 2) identifying the mechanisms impacting the microstructural changes and the hardness properties within the weld. A similar quantitative approach has been performed in this paper on the near- $\alpha$  Ti6242. However the article will focus on using the crystallographic information from the martensitic as-welded (AW) microstructures to reconstruct the high temperature  $\beta$  microstructure before cooling. The information gathered will permit to design a PWHT that ensures equilibrium in the joint, smooth microstructure transitions **without any changes in the as-received microstructure, or in the hardness of the base material**. The characteristic

LFW macro-zones will be investigated by Optical Microscopy (OM), Scanning Electron Microscopy (SEM), Electron Back-Scattered Diffraction (EBSD), X-Ray Diffraction (XRD) and micro-hardness measurements. The results of monotonic tensile tests and fatigue behavior characterization on the as-welded configuration are reported by others in [17].

## 2. MATERIAL AND METHODS

The LFW equipment used was a MDS-30 developed by the company ACB, Nantes, France. The samples were welded using: a forging pressure of 90 MPa, an oscillating motion amplitude and frequency of 2 mm and 50 Hz, respectively, and a threshold in the axial shortening of 3 mm. The temperatures experienced during the process were measured by nine INCO sheathed thermocouples on each part (forging and oscillating) placed centrally (i.e. at a depth of 7.5 mm) and initially located at 2, 4, 6 and 8 mm from the contact surface.

Blocks of 15\*80\*70 mm<sup>3</sup> were obtained by electrical discharge machining from a forged billet (R=250 mm ; L=570 mm) of TIMETAL®6-2-4-2 with the 80 mm edge parallel to the billet axis. The material was provided in the solution treated then aged configuration (STA) by TIMET Savoie S.A., France. The specimen were welded on the raw 15\*80 mm<sup>2</sup> surface, the 80 mm edge being aligned with the oscillation direction (see Figure 1a). In Figure 1b the flash of expelled material along <x> and <y> can be clearly seen. The samples dedicated to microstructural characterization were cut across the weld ensuring a sample height about 10 mm on either side of the weld center line (Figure 1a). The specimens were polished using the following papers at 100 rpm: P80, P220, P1200, P2400, and P4000; the papers above grade 1000 were used twice for 30 s

each. Surface finishing required using polyester cloth polishing, first with a 6  $\mu\text{m}$  diamond suspension then with a Struers oxide polish suspension (OPS) for 2 min each at 100 rpm. Vibratory polishing was performed for EBSD investigations using a solution composed by 50 ml of OPS and 50 ml of  $\text{H}_2\text{O}$  on a Buehler VibroMet 2 for 48 h under a load of 200 g. Optical microscopy required the use of an etchant for 12 s at room temperature with the following composition: 2 ml HF, 98 ml  $\text{H}_2\text{O}$  [18].

Macro-scale analysis was performed using both an OM Olympus BX41M and a micro-hardness machine Zwick-Roell ZHU $\mu$ -S. Micro-scale observations were performed on a Zeiss Sigma SEM (at 15 kV) coupled with an EBSD system (at 25 kV). The crystallographic investigations were carried out on a Bruker D8 ADVANCE Twin X-Ray diffractometer using a Cu source at 20 kV/40 mA through a 0.1 mm slit with symmetrical beam path. Electrical-tape masks were used to irradiate only the areas of interest. The PWHTs were performed using a Nabertherm P330 oven under an Argon protective atmosphere.

The Matlab $\text{\textcircled{C}}$  tool box Mtex 5.1.1 was used for post-processing the EBSD data and for reconstructing the  $\beta$  orientations at high temperatures prior to the martensitic transformation with self-developed subroutines. The XRD diffractograms were post-processed using the software Diffrac.Eva $\text{\textcircled{C}}$ .

Figure 1 : a) Sketch of the geometry of the welded parts and the sampling method for observations and diffraction analysis [16] with the forging direction  $\langle z \rangle$  and the oscillating direction  $\langle y \rangle$ ; b) picture of the whole assembly. The forging part is the upper part ( $z > 0$ ) and the oscillating part is the lower part ( $z < 0$ ).

### 3. RESULTS AND DISCUSSIONS

#### 3.1. MICROSTRUCTURE OF THE BASE MATERIAL

The base material near- $\alpha$  Ti-6Al-2Sn-4Zr-2Mo in the as-received, fully-equiaxed state is characterized by predominant textured nodular primary  $\alpha$  ( $\alpha_p$ ) grains (90 vol.%) within a  $\beta$  matrix (10 vol.%) (Figure 2). This microstructure results from  $\beta$  thermo-mechanical processing forming large recrystallized  $\beta$  grains followed by lamellar  $\alpha$  precipitation upon cooling; then  $\alpha+\beta$  forging steps are performed to obtain globularization through lamellar break down of the  $\alpha$  colonies [19]. The fully-equiaxed Ti6242 in this study is characterized by a  $\beta$ -transus of 990 °C, a yield strength and ultimate tensile stress of 895 MPa and 1018 MPa, respectively, with an elongation at fracture of 19%. Quenching the fully-equiaxed Ti6242 from the  $\beta$  domain forms entangled  $\alpha'$  martensitic laths precipitated within prior- $\beta$  grains; fast cooling from the  $\alpha+\beta$  domain forms a bimodal microstructure made of shrunk  $\alpha_p$  nodules and lamellar secondary  $\alpha$  ( $\alpha_s$ ) precipitated within transformed  $\beta$  ( $\beta_t$ ) zones [1], [2], [20].

Figure 2 : Fully-equiaxed microstructure of the as-received Ti6242 base material. SEM micrographs of the  $\alpha_p$  nodules in dark grey (marker #1) within the bright  $\beta$  matrix (marker #2).

#### 3.2. MACROSCALE ANALYSIS OF A WELDED SPECIMEN

An overall micrograph of the Ti6242 LFW joint is displayed in Figure 3. Friction heating combined with the forging pressure made the viscous material to flow out of the

assembly, into the flash, mainly on the long sides of the sample (as also seen in Figure 1b). A significant curvature of the joint can be noted which is characterized by a point symmetry at the weld center. This particular joint morphology is associated with a remarkable asymmetry between both transversal flashes. Both features could be resulting from an initial misalignment of the two parts prior to welding (seen by the offset of the parts in the welded state) which might have affected considerably the material flow during the process. The total LFW process time lasted 1,35 s with an axial shortening of 3,31 mm.

Figure 3 : Preliminary inspection of the weld by OM after etching revealing an offset in the alignment of the parts along  $x$ , asymmetrical flashes and the curvature of the joint.

Temperature measurements shown in Figure 4a were conducted at 7.5 mm in depth (i.e. in the center of the specimen) across the weld and initially placed at 2, 4, 6 and 8 mm from the contact surface, their initial positions are detailed in Figure 4b. Only one LFW test was instrumented for qualitative temperature investigations.

Figure 4 : Temperature measurements across the joint showing a) the thermocouple data from the forging part and the oscillating part; b) the initial thermocouple positions. The colors indicate the initial distance from the contact surface prior to axial shortening: TC1+5+9, TC3+7, TC2+8 and TC4+6 were placed at 2 mm, 4 mm, 6 mm and 8 mm, respectively.

The temperature data in Figure 4 showed that solely the thermocouples TC1+5+9, the closest to the weld center line, experienced a local  $\beta$  thermo-mechanical processing characterized by a brisk heating to 1200 °C (1000 K/s) followed by fast cooling (-80 K/s). However one can notice important differences between TC5 at the center and TC1+9 at the edges in terms of their cooling rates as the core cooling was much slower than the ones on the sides. This heterogeneity could have a major impact on larger parts concerning microstructure changes and residual stresses. The second and third rows of thermocouples (namely TC3+7 and TC2+8) recorded similar symmetric maximum temperatures delayed from the end of the oscillations. This delay increases and the local maximum temperature decreases when getting farther from the interface as expected from heat conduction. Furthermore, a rather pronounced {xz} mirror symmetric behavior can be noted between the opposite thermocouples TC1+9, TC3+7 and TC2+8 in both welded parts indicating a probable {xz} mirror symmetry in the heat flux. Yet both fourth rows of thermocouples (TC4+6) were subject to anomalies which might result from the deterioration of the thermocouple connection during the process. Due to the axial shortening by material extrusion, the z position of the thermocouples changed during the process resulting in the TC1+5+9 of the front rows to be approximately at 0.5 mm from the weld center line at the end of the process. A rather symmetrical axial shortening have been noted between the forging part and the oscillating part. Combining the temperature data with the axial shortening enabled the identification of the local temperature maxima depending on the final distance of a material point from the weld center line. These data in Figure 5 revealed that a band of approximately  $\pm 1$  mm from the interface reached the  $\beta$ -transus of 990 °C and above with a dwell time in the  $\beta$  domain about 2.5 s. A band of approximately  $\pm 2$  mm experienced temperatures above 700 °C critical for the start of a (partial)  $\alpha \rightarrow \beta$  transformation [20], [21].

Figure 5 : Local temperature maxima measured by the thermocouples (black dots) in dependence on the final distance from the weld center line after axial shortening combined with the local dwell time in the  $\beta$  domain experienced during the process (red triangles).

The joint observation by polarized-light OM before etching in Figure 6 highlighted the presence of a strong microstructure heterogeneity between the base material and the joint. A sharp transition has been identified from the equiaxed initial microstructure to a region with microstructure refinement starting 800  $\mu\text{m}$  from the weld center line. This central zone named the Thermo-Mechanically Affected Zone (TMAZ) seemed to exhibit a continuous grain refinement similar to nodule fragmentation. However, such an abrupt microstructure change could not be observed any longer after etching, but it allowed to reveal the subdivision of this central fragmented-like zone into three sub-zones: the narrow **Welding Line (WL)** of 60  $\mu\text{m}$  in width made of fine laths within recrystallized-like equiaxed grains (with grain diameter about 5  $\mu\text{m}$ ); highly deformed  $\alpha$  nodules in the near-TMAZ (NTMAZ) of 300  $\mu\text{m}$  in width, **and the far-TMAZ (FTMAZ) up to a width of 800  $\mu\text{m}$ . An antagonism exists with the FTMAZ looking just plastically affected on the etched sample while exhibiting a remarkable microstructure refinement under polarized-light.**

Figure 6 : Combined data from OM observations with polarized-light and corresponding local hardness across the Ti6242 LFW joint detailing the characteristic macro-zones: the Welding Line (WL), the Thermo-mechanically Affected Zone (TMAZ) and the Heat Affected Zone (HAZ). The polarized-light showed the global microstructure refinement

in the joint and etching revealed a further subdivision of the TMAZ into the far-TMAZ (FTMAZ) just deformed, the near-TMAZ (NTMAZ) heavily deformed and the WL fully transformed.

These microstructure changes result in a significant gradual increase in hardness in the joint with a sharp maximum in the WL (a 40% increase). A third weld zone characterized by a microstructure similar to the one of the base material but displaying slightly higher hardness values has also been identified as the Heat Affected Zone (HAZ) of 800  $\mu\text{m}$  in width connecting the base material and the TMAZ. The total Process Affected Zone (PAZ) width is thus about  $\pm 1.6$  mm on either side of the weld center line and slightly thinner (by 20%) than expected from the temperature fields.

The temperatures recorded in this study were in the same order of magnitude of 1000 °C as identified in [22], [23] for LFW of Ti-6Al-4V. Comparable microstructures have been identified in [10]–[13] on LFW welds of near- $\alpha$  Ti-alloys with a similar weld hardening. Cross-checking the results from OM and micro-hardness data was fundamental to precisely identify the positions of the characteristic macro-zones of this joint despite the temperature data. However, it only suited preliminary identifications of the major microstructural changes. The limited information that can be extracted from those methods solely do not allow any proper characterization of the thermo-mechanical load accommodation mechanisms, nor of the crystallographic changes that happened in the joint during LFW. The following sections are thus dedicated to the microscale characterization of the three macro-zones forming the PAZ with the use of SEM, EBSD and XRD. The information gathered in these sections will be crucial for designing the specific PWHT.

### 3.3. MICROSTRUCTURAL AND CRYSTALLOGRAPHICAL ANALYSIS OF THE CHARACTERISTIC ZONES OF THE JOINT

High magnification observations by SEM in Figure 7 showed the important changes in the microstructure across the weld. The WL is characterized by thin laths precipitated within fine equiaxed grains without any traces of plastic deformation (the discussion will be the subject of the specific section 3.4.2.). On the contrary, the NTMAZ exhibits a severely deformed prior-nodular microstructure, this aspect is diminished when approaching the FTMAZ as well as a gain in contrast with respect to the retained inter-nodular  $\beta$  matrix. Furthermore, the image contrasts suggest that the  $\alpha$  grains are progressively fragmented and/or transformed in the TMAZ with traces of fine-lath networks formed within the former  $\beta$  matrix in the NTMAZ. Just deformed fragmented-like former  $\alpha_p$  within a clear  $\beta$  matrix can be observed in the FTMAZ. Attentive observations at the core of the weld revealed the presence of fine defects and/or porosities at the supposed center of the WL shown in Figure 8. These porosities, highly detrimental to fatigue resistance, have already been reported in [17] and were attributed to the shrinkage of microscopic liquid pockets. A local enrichment in copper and zinc from electrical discharge machining was believed to cause this liquefaction.

Figure 7 : Microscale observations by SEM in Back-Scatter Electron (BSE) mode of the joint showing the microstructures in the different zones within the joint a) WL: ultra-fine laths (1) precipitated within fine equiaxed grains (2); b) NTMAZ: highly deformed  $\alpha$  nodules (3) and transformed “Ghost” prior- $\beta$  matrix (4); c) FTMAZ: slightly deformed  $\alpha$  nodules with traces of fragmentation (5) and retained  $\beta$  matrix (6).

Figure 8 : Microscale observations by SEM in Back-Scatter Electron (BSE) mode of the center of the WL showing the presence of defects/porosities along the central line.

Additional EBSD analysis of the HCP phase across the joint in Figure 9 revealed a considerable microstructure refinement involving different mechanisms **in the three macro-zones of the joint**: the WL, the NTMAZ and the FTMAZ. The zoom in the WL in Figure 9b showed the formation of fine HCP entangled laths in the WL corroborating the SEM observations; no traces of prior- $\beta$  grains were identifiable here. The FTMAZ fragmented-like microstructure in Figure 9d displayed fine  $\alpha$  precipitates together with coarse  $\alpha$  grains slightly smaller than the  $\alpha$  nodules in the base material coexisting with residual  $\beta$  matrix. The NTMAZ microstructure in Figure 9c appeared to be a hybrid between the two previously depicted microstructures by exhibiting a very fine acicular microstructure interspersed with highly deformed residual nodules. However, the super fine laths formed within the former  $\beta$  matrix in the NTMAZ could not be indexed.

Figure 9 : EBSD orientation map of the HCP phase (step size=0.3  $\mu\text{m}$ ) within the joint highlighting a) the microstructure refinement at the TMAZ/HAZ border ( $z\approx 800\ \mu\text{m}$ ) and the change of microstructure in the joint from fragmented-like in the TMAZ to acicular in the WL. The arrows indicate the positions of the three magnified local regions b) WL HCP entangled laths; c) NTMAZ squeezed/shrunk prior-nodular  $\alpha$  and fine laths; d) FTMAZ showing fragmented-like coarse prior-nodular  $\alpha$  within a  $\beta$  matrix (grey). The colors indicate the crystallographic directions of the HCP phase along the  $\langle x \rangle$  direction. Grains formed by less than five measurement points were considered as not indexed.

A specific feature could be noted in the FTMAZ as some fine  $\alpha$  precipitates appeared to share clear Burgers Orientation Relationship (BOR) with the adjacent  $\beta$  phase. The results in Figure 10 showed that notable  $\langle 0001 \rangle_{\alpha} // \langle 110 \rangle_{\beta}$  and  $\langle 11\bar{2}0 \rangle_{\alpha} // \langle 111 \rangle_{\beta}$  alignments could be identified between the tested  $\beta$  grain and its  $\alpha$  neighbors (40  $\alpha$  grains). Such a BOR between the  $\alpha$  nodules and the  $\beta$  matrix could not be found in the base material due to lamellar breakdown.

Figure 10: EBSD analysis in the FTMAZ highlighting of the Burgers Orientation Relationship ( $\{0001\}_{\alpha} // \{110\}_{\beta}$  ;  $\langle 11\bar{2}0 \rangle_{\alpha} // \langle 111 \rangle_{\beta}$ ) between the  $\beta$  matrix (green) and neighboring  $\alpha$  fragments (blue) showing in a) a selected  $\beta$  grain marked by the symbol  $\beta$  and its neighbors (outlined by white boundaries); b)-c) overlaid 110-0001 and 111-11 $\bar{2}0$  pole figures of the mean grain orientations of the reference  $\beta$  grain (red stars) and its  $\alpha$  neighbors (black dots).

One can also notice an occurring texture in the HCP orientation map in Figure 9a which has been confirmed by plotting the 0001 and 11 $\bar{2}0$  pole figures in Figure 11. This texture is characterized by the gradual formation of one dominating texture component when approaching the WL from the oscillating FTMAZ. The most frequent texture component in the WL is  $\{0001\} \langle 11\bar{2}0 \rangle$  with the  $\{0001\}$  plane slightly misaligned with the transversal plane  $\{xz\}$  and the  $\langle 11\bar{2}0 \rangle$  direction along the main material expulsion direction  $\langle x \rangle$ . Nevertheless no particular texture was observed past 600  $\mu\text{m}$  from the weld center line.

Figure 11 : Local texture analysis of the HCP phase from the orientation map in Figure 9 through 0001 and  $11\bar{2}0$  pole figures obtained from: a)  $z = [50 ; -50] \mu\text{m}$  (WL); b)  $z = [-150 ; -250] \mu\text{m}$  (oscillating NTMAZ); c)  $z = [-350 ; -450] \mu\text{m}$  (oscillating FTMAZ); d)  $z = [-550 ; -650] \mu\text{m}$  (oscillating FTMAZ). The orientation density function was obtained from the measured orientations using a half width of  $2^\circ$  and used to plot the pole figures with a minimum of 120 000 orientations (10000 and 3000 grains in the WL and in the TMAZ, respectively).

Complementary crystallographic analysis by XRD across the joint performed on a  $\{yz\}$  central surface with the diffraction vector aligned with  $\langle x \rangle$  in Figure 12 verified the absence of  $\beta$  phase in the core of the joint (WL+NTMAZs) with strong similarities with the  $\alpha'$  martensitic microstructure obtained by water quenching the base material from the  $\beta$  domain. A similar analysis conducted in the FTMAZ showed the presence of the  $\beta$  phase in this zone corroborating the EBSD data. One can also notice an increased peak width in the FTMAZ compared to the base material in as-received condition (BM AR) which could result from the grain size broadening due to microstructure refinement. The abnormal intensity of the 0002 peak observed in case of WL+NTMAZs suggests the presence of a texture component with  $\langle 0001 \rangle$  along the  $\langle x \rangle$  direction additional to the  $\{0001\}\langle 11\bar{2}0 \rangle$  texture component of the WL. This apparent contradiction to the EBSD texture analysis of the WL is caused by the much larger information volume in XRD including the adjacent layers of the NTMAZs which exhibits such a 0001 pole close to  $\langle x \rangle$ . The low thickness of the WL did not allow the authors to analyze the WL separately from the adjacent NTMAZs by XRD.

Figure 12 : XRD diffractograms of restricted ranges of the diffraction angle of the core of the joint (WL+NTMAZs) and the FTMAZ compared to the base material water-quenched (BM WQ) sample and the base material as-received (BM AR). The surface irradiated is {yz}.

### **3.4. THERMO-MECHANICAL LOAD ACCOMODATION MECHANISMS ACROSS THE WELD**

#### **3.4.1. PHASE TRANSFORMATIONS AND MICROSTRUCTURE REFINEMENT**

The main consequence of the LFW process on the joint is the heterogeneous partial/complete  $\alpha \rightarrow \beta$  phase transformation due to gradients of the thermo-mechanical processing conditions leading to significant microstructural changes. These gradients resulted in the formation of macro-zones distinguishable by sharp microstructure transitions as well as different hardness properties. The thermocouple data suggested that a central band about  $\pm 1$  mm along  $\langle z \rangle$  experienced temperatures above the  $\beta$ -transus (990 °C) followed by quenching. One could expect from the literature [1], [2] that such a heat treatment should have turned the whole central band into a fully transformed martensitic microstructure. However the phase identification by EBSD and XRD showed solely the joint core (WL+NTMAZs) to exhibit strong correlations with the  $\alpha'$  martensitic microstructure obtained in the water quenched sample. Indeed it has been proven by [24], [25] that a substantial superheat above the conventional  $\beta$ -transus

is required to complete the  $\alpha \rightarrow \beta$  transformation in zones that endured high heating rates (500-1000 K/s) during gas tungsten arc welding of Ti-6Al-4V. Furthermore the identification of coarse deformed former  $\alpha_p$ -like nodules in the NTMAZ could be a marker of a partial  $\alpha + \beta \rightarrow \alpha + \alpha'$  transformation, so that solely the WL might have undergone a complete  $\alpha \rightarrow \beta$  transformation. Thus the authors, with the help of EBSD and  $\beta$  reconstruction algorithms, will provide crucial information about phase transformation and microstructural refinement in LFW Ti6242. A quantitative analysis of the EBSD data concerning the features of  $\alpha/\alpha'$  grains and the  $\beta$  phase area fraction summarized in Figure 13 confirmed the microstructural refinement in the TMAZ visible by OM with polarized light. At the HAZ/TMAZ border a sharp local drop in the grain diameter occurs. Those changes in the grain features are accompanied by a gradual decrease in the volume fraction of the  $\beta$  phase throughout the FTMAZ; the absence of  $\beta$  phase in the WL and the NTMAZ is confirmed corroborating the XRD measurements.

Figure 13 : Evolution of the  $\alpha/\alpha'$  grain diameter (longest distance between any two pixels along the grain boundary) and aspect ratio (length/width) combined with the local  $\beta$  phase area fraction across the joint (along  $\langle z \rangle$ ) showing an abrupt microstructural refinement at the TMAZ/HAZ border, a gradual loss of  $\beta$  phase in the FTMAZ and its total absence in the WL and the NTMAZ.

Complementary analysis on the cumulated misorientation angle distribution at the  $\alpha/\alpha'$  grain boundaries plotted in Figure 14 also revealed a significant microstructure change in the joint from the base material features, the trends appeared in fact quite similar to the  $\alpha'$  of the water quenched sample. Indeed the data from the WL, NTMAZ

and FTAMZ also showed steps on the curves at the characteristic angles of  $60^\circ$  and  $90^\circ$ . Such distributions are analogous to the ones obtained from the  $\beta \rightarrow \alpha$  variant selection during the  $\beta \rightarrow \alpha'/\alpha_s$  transformation within a single  $\beta$  parent grain in [26], thus indicating a probable microstructure refinement by  $\beta \rightarrow \alpha$  variant selection relying on BOR. However the differences with the water quenched sample with respect to the occurrence of small misorientations might be due to two effects in the joint: 1) the fragmentation of prior- $\beta$  grains which increases the frequency of common boundaries between  $\alpha$  laths precipitated from different  $\beta$  parent grains; 2) an increase in poorly indexed regions jeopardizing the theoretical stepped curve. The HAZ exhibited a microstructure and cumulated misorientation angle distribution comparable to the ones of the base material as-received (BM AR) corroborating the threshold effect of the microstructural refinement.

Figure 14 : Cumulated correlated misorientation angle distributions across the boundaries between  $\alpha/\alpha'$  grains in the different joint zones compared to the base material as-received (BM AR) and the water-quenched sample (BM WQ). The kinks at  $60^\circ$  and  $90^\circ$  are typically observed between  $\alpha$  variants precipitated from a common  $\beta$  parent orientation. The zones investigated were taken from the orientation data in Figure 9 from the oscillating part at the following  $\langle z \rangle$  positions in  $\mu\text{m}$ : [50 ; -50], [-150 ; -250], [-550 ; -650] and [-950 ; -1050] for the WL, NTMAZ, FTMAZ and the HAZ, respectively. A threshold of  $2^\circ$  was used for grain boundary detection. The data of the water-quenched sample were obtained from 4780  $\alpha'$  laths precipitated within the same prior- $\beta$  parent grain. The data of the base material as-received were obtained from 2210  $\alpha_p$  nodules from a single  $4 \cdot 10^3 \mu\text{m}^2$  macro-zone.

Local orientation observations in the FTMAZ revealed that most “fragments” constituting different former  $\alpha_p$  nodules had orientations whose specific  $\langle 0001 \rangle$  and  $\langle 11\bar{2}0 \rangle$  directions were collinear to  $\langle 110 \rangle$  and  $\langle 111 \rangle$  directions of the adjacent  $\beta$  matrix respectively. This indicated probable orientation relationships inherited from a common  $\beta$  parent grain through the BOR. As a result the authors proposed here to reconstruct the prior- $\beta$  orientations of clusters that share a common  $\beta$  parent to identify the contribution of the  $\alpha \rightarrow \beta \rightarrow \alpha' / \alpha_s$  phase transformation to the microstructure refinement. To do so, an algorithm based on the work of [27]–[30] for prior-austenitic grain reconstruction from martensitic clusters has been developed which relies on the following major steps: 1) finding each local  $\alpha / \alpha'$  cluster containing at least three neighboring laths separated by grain boundaries with misorientations above  $15^\circ$ ; 2) computing each possible  $\beta$  parent orientation for each HCP orientation ensuring the BOR  $\{0001\}_\alpha // \{110\}_\beta$  and  $\langle 11\bar{2}0 \rangle_\alpha // \langle 111 \rangle_\beta$ ; 3) comparing the  $\beta$  parent orientations of a reference lath with the orientations of the other laths of the cluster; 4) assigning to this reference lath the  $\beta$  orientation ensuring a minimum average misorientation among the solutions that have at least two neighbors with misorientation angles lower than  $4^\circ$ ; 5) repeat steps 3-4 for each lath in a cluster and 6) steps 2-5 for each cluster. The  $\alpha / \alpha'$  laths and fragments dissatisfying these conditions were classified as unreconstructable grains. The Matlab© scripts using the Mtex 5.1.1 tool box were tested and validated on clusters of entangled  $\alpha$  lamellae within large prior- $\beta$  equiaxed grains ( $D=1$  mm) of a Ti17 Widmanstätten  $\alpha + \beta$  microstructure.

Figure 15 : Orientation map of the BCC  $\beta$  phase obtained by parent grain reconstruction from the  $\alpha/\alpha'$  clusters shown in Figure 9 combined with the experimental retained  $\beta$  matrix displaying: the significant area fraction of  $\alpha$  “fragments” sharing common  $\beta$  parents in the TMAZ associated with a gradual  $\beta$   $\langle 111 \rangle$  texture development in the NTMAZ and a noticeable prior- $\beta$  grain fragmentation in the WL. The color indicates the crystallographic directions of the BCC  $\beta$  phase along the  $\langle x \rangle$  direction. The white lines represent grain boundaries with a misorientation angle above of  $5^\circ$ . The grey color indicates unreconstructable fragments.

The result of the reconstruction shown in Figure 15 revealed that, contrary to the base material as-received and the HAZ, the algorithm identified a significant area fraction of  $\alpha/\alpha'$  grains sharing common  $\beta$  parents in the joint. Different features across the WL/NTMAZ and the FTMAZ can be noticed: the WL and the NTMAZ are characterized by much fewer unreconstructable  $\alpha$  fragments (6% vs. 20% of the indexed data for the WL/NTMAZ and the FTMAZ, respectively) and the development of a strong texture with  $\langle 111 \rangle$  along  $\langle x \rangle$  associated with the visible formation of subgrains within deformed large prior- $\beta$  grains. A retro analysis of the misorientation angle frequency over the  $\alpha/\alpha'$  grain boundaries in the joint separating the reconstructable fragments from the unreconstructable ones is shown in Figure 16. The distribution for the unreconstructable  $\alpha$  grains revealed the absence of kinks, but a rather continuous increase remarkably different from the distribution of the reconstructable ones. Furthermore the distribution of the reconstructable fragments appeared remarkably similar to the angle distribution for random variant selection from a single  $\beta$  parent grain thus corroborating the microstructural refinement by  $\beta \rightarrow \alpha$  variant selection.

Figure 16 : Cumulated correlated misorientation angle distributions excluding the reconstructable fragments (solid red) from the unreconstructable ones (solid black) compared to uncorrelated distribution of random orientations (dashed black). 650 unreconstructable  $\alpha$  grains were used in the analysis.

Comparing the SEM and XRD observations with the reconstructed high temperature  $\beta$  microstructure confirmed that actually both the WL and the NTMAZs underwent a complete  $\alpha \rightarrow \beta$  transformation during the process. The few remaining unreconstructable grains were assumed to be due to a 3D effect where the  $\alpha'/\alpha$  lath matching would be found above or below the observed surface. The combined results from the  $\beta$  reconstruction, the boundary misorientation data and the clear BOR between the  $\beta$  matrix and neighboring  $\alpha$  fragments suggest that the FTMAZ experienced local thermo-mechanical loads that might be similar to a conventional  $\alpha+\beta$  processing ( $T > 700$  °C). The latter is known to refine the fully-equiaxed microstructure into a duplex/bimodal one as depicted in [31]–[34]. Furthermore the shear strains experienced in the TMAZ during LFW associated with the local shear induced by the  $\beta_t \rightarrow \alpha_s$  transformation upon cooling might have enhanced the fragmentation of the remaining  $\alpha_p$  nodules into unreconstructable fragments. The presence of retained  $\beta$  matrix after fast cooling in the FTMAZ might be due to a combination of two effects: the lack of time at high temperatures associated with a poor material mixing. These would lead to a negligible redistribution of  $\beta$ -stabilizing elements into the bulk thus jeopardizing the common duplex-microstructure formation ( $\alpha_s$  lamellae interspersed with scattered  $\beta$  spots).

### 3.4.2. MATERIAL FLOW AND RECRYSTALLIZATION

The traces of fine equiaxed grains revealed by SEM observations combined with the misorientation angle distribution of the  $\alpha'$  laths in the WL led to the proposal that the martensitic laths precipitated within fragmented prior- $\beta$  grains in the joint core. This suggestion was corroborated by the computation in Figure 15 showing a visible subgrain formation within deformed prior- $\beta$  grains in the WL. A preliminary analysis was conducted on the misorientation angles (correlated between neighboring grains and uncorrelated between randomly chosen grains). The results are displayed in Figure 17a combined with the computed  $\beta$  texture within the WL and the NTMAZ presented as pole figures in Figure 17b and Figure 17c respectively.

Figure 17 : a) Correlated misorientation angle distributions across the boundaries of the reconstructed prior- $\beta$  grains and the corresponding uncorrelated misorientation angle distributions in the WL, the oscillating NTMAZ and the oscillating FTMAZ; recalculated 110 and 111 pole figures of the reconstructed prior- $\beta$  grains in b) the WL and c) the oscillating NTMAZ. With decreasing distance from the weld center, i.e. from the FTMAZ to the WL, first an increase in the frequency of low misorientation angles at the expense of higher misorientation angles is observed, followed by a slight decrease in favor of boundaries with very high angles. These high fraction of boundaries with very high angles are a consequence of the developing texture from one dominating component towards two dominating components. A threshold of  $5^\circ$  was used for grain boundary detection and halfwidth of  $5^\circ$  was set for the orientation distribution function calculation.

The analysis in Figure 17a revealed a significant increase in the frequency of low misorientation angles between the oscillating FTMAZ and the oscillating NTMAZ. This effect might be due to re-orientation of the  $\beta$  grains during deformation towards an ideal orientation properly aligned with the deformation conditions [35]. Indeed a single  $\{110\}\langle 111\rangle$  texture component (with a  $\langle 111\rangle$  direction along  $\langle x\rangle$  and a  $\{110\}$  plane as  $\{xy\}$  plane) can be observed in the oscillating NTMAZ in Figure 17c corroborating the increase in frequency of low misorientation angles at the expense of the higher angles. The WL, on the contrary, appeared to be defined by two main twin-symmetric  $\{110\}\langle 111\rangle$  texture components as seen from the pole figures showed in Figure 17b. However solely one could be identified as coming from the NTMAZ of the oscillating part requiring a detailed local analysis for revealing the origin of the twin-symmetric component ( $\beta_{\text{TWIN}}$ ). To do so, a preliminary approach was to compare the ideal reconstructed orientations of the  $\beta$  phase from the WL to the ones from the forging and the oscillating NTMAZs in the pole figures displayed in Figure 18.

Figure 18 : Local analysis of the BCC  $\{hkl\}\langle 111\rangle$  texture development among the prior- $\beta$  grains close to the weld center line relying on the reconstructed  $\beta$  orientations ( $\beta^{\text{Rec}}$ ) from the experimental  $\alpha/\alpha'$  orientations ( $\alpha^{\text{Exp}}$ ). The 0001 and  $11\bar{2}0$  pole figures of the  $\alpha^{\text{Exp}}$  are plotted for a) the forging NTMAZ ( $\alpha_{\text{FRG}}$ ); b) the WL ( $\alpha_{\text{WL}}$ ) and c) the oscillating NTMAZ ( $\alpha_{\text{OSC}}$ ). The corresponding 110 and 111 pole figures of the  $\beta^{\text{Rec}}$  are plotted in d)-f). Four ideal orientations are marked, one for each of the NTMAZ ( $\beta_{\text{FRG}}$  on the forging side in blue and  $\beta_{\text{OSC}}$  on the oscillating side in red) and two in the WL (a local component  $\beta_{\text{WL}}$  in purple and the corresponding twin component  $\beta_{\text{TWIN}}$  in green).

Inspection of the experimental  $\alpha/\alpha'$  HCP orientations from the joint core revealed that the texture of the pole figure of the two opposing NTMAZs appeared significantly similar, but characterized by a  $30^\circ$  rotation around the  $11\bar{2}0$  pole aligned with  $\langle x \rangle$ . Furthermore an extensive study of the distribution of the poles revealed that each NTMAZ seemed to be composed of a single dominant texture component of the  $\beta$  phase prior to cooling, moreover also mutually rotated by  $30^\circ$ . The orientation reconstruction of the  $\beta$  phase from the  $\alpha/\alpha'$  data points confirmed the presence of solely one dominating  $\{hkl\}\langle 111 \rangle$  texture component in each NTMAZ, namely  $\beta_{\text{FRG}}$  and  $\beta_{\text{OSC}}$  in the forging part and the oscillating part, respectively. All these  $\{hkl\}\langle 111 \rangle$  components have a  $\langle 111 \rangle$  direction in common aligned with  $\langle x \rangle$ , but differ in their crystallographic plane  $\{hkl\}$  aligned with the  $\{xy\}$  plane (i.e. the forging plane). Where the forging NTMAZ shows solely the  $\{110\}\langle 111 \rangle$  texture component, an apparent  $\{112\}\langle 111 \rangle$  texture component might be noted in the oscillating NTMAZ. The latter is actually equivalent to the  $\{110\}\langle 111 \rangle$  texture component from the forging NTMAZ rotated by  $30^\circ$  around  $\langle 111 \rangle$ . This interesting asymmetry is resulting from the alignment of the local  $\{110\}\langle 111 \rangle$  slip system to different planes and directions: in the forging NTMAZ the  $\langle 110 \rangle$  direction is aligned with the forging direction  $\langle z \rangle$  and in the oscillating NTMAZ the  $\langle 110 \rangle$  direction is aligned with the oscillating direction  $\langle y \rangle$ . The observed misorientation angle of  $30^\circ$  is a direct consequence of this shifting alignment taking into account crystal symmetry; the two different alignments might result from an asymmetric plastic behavior between the forging and the oscillating part during LFW. Furthermore, one of the two orientations of the  $\beta$  phase present in the WL ( $\beta_{\text{WL}}$ ) appeared to be just the intermediate between these two components of the two NTMAZs due to an overlapping effect. The spatial distribution of the ideal orientations combined with the local misorientation to the reference are shown in Figure 19.

Figure 19 : Spatial distribution of the three main  $\{hkl\}\langle 111 \rangle$  texture components of the  $\beta$  phase (i.e.  $\beta_{FRG}$ ,  $\beta_{OSC}$ , and  $\beta_{TWIN}$ ) combined with the local angular deviation from the closest reference orientation. The recrystallized nuclei highlighted by white boundaries were identified as having at least one boundary with a misorientation above  $15^\circ$  and ensuring a grain orientation spread lower than  $1^\circ$ . The white dashed line represents the weld center line (WCL).

A sharp border can be observed in Figure 19 between the two sides of the weld (i.e forging and oscillating) and the local misorientations to the ideal parent orientation showed the absence of any gradual crystal rotation from one part to the other. Solely a random orientation spread from the ideal orientations could be observed ( $10^\circ$  and  $8^\circ$  for the forging and the oscillating part, respectively). The twin component  $\beta_{TWIN}$  which is twin-symmetric to  $\beta_{WL}$  appeared to be mostly present in the oscillating part in the form of large clusters and as scattered fine grains in both NTMAZs. An analysis along the WL from a band of  $700 \times 50 \mu\text{m}^2$  identified an even blending of  $\beta_{WL}$  and  $\beta_{TWIN}$  (as defined in Figure 18e) within the joint center line characterized by an area fraction of 45% of  $\beta_{WL}$ , 44% of  $\beta_{TWIN}$  and 11% of unrelated orientations. This texture blending could be caused by a local interpenetrating material flow mixing of the two single-component textures coming from the forging and the oscillating NTMAZs.

Such a material mix could be of major importance as: 1) it could enhance the  $\beta$ -stabilizing element redistribution in the bulk explaining the differences of microstructure noted by SEM between the WL and the NTMAZ (“Ghost”  $\beta$  in the NTMAZ); 2) it might have an influence on the defect redistribution impacting the weld

quality. Material stirring and the related plastic deformation could also be responsible for the significant increase in frequency observed at the misorientation angle of  $60^\circ$  in the WL compared to the NTMAZ (in Figure 17a) through recrystallized nuclei formation in twin orientation and the generation of  $\beta_{WL}/\beta_{TWIN}$  boundaries. Indeed large deformation could lead to such an apparently recrystallized microstructures due to a phenomenon called continuous dynamic recrystallization (CDRX) [36], [37] by grain subdivision or fragmentation forming large misorientation boundaries as depicted in [38], [39].

The recrystallized nuclei drawn in Figure 19 within the stirred microstructure and the corresponding 110 and 111 pole figures for each weld side plotted in Figure 20 revealed the following major features: 1) the nuclei are scattered across the WL and the NTMAZs; 2) The nuclei orientations are mainly related to the local ideal orientations but slightly rotated; 3) a recrystallized area fraction of 16% was identified with a mean nuclei diameter of  $9 \mu\text{m} \pm 3 \mu\text{m}$ . In addition to that the asymmetric behavior identified through local texture development is also visible in terms of recrystallization features as: 1) the nuclei rotation from the ideal orientations appeared to be much more remarkable in the oscillating part compared to the forging side; 2) the oscillating part exhibits a higher recrystallized area fraction (17% vs. 14%) with slightly smaller nuclei diameter ( $8.8 \mu\text{m}$  vs.  $9.2 \mu\text{m}$ ).

Figure 20 : 110 and 111 pole figures of the mean orientation of all recrystallized nuclei for a) the forging part and b) the oscillating part. The ideal orientations  $\beta_{FRG}$ ,  $\beta_{OSC}$  and  $\beta_{TWIN}$  are shown in blue, red and green stars respectively.

Preceding studies on LFW of near- $\alpha$  Ti-alloys proposed that dynamic recrystallization might have happened in the WL and in the NTMAZs resulting in a similar grain size [10]–[14]. Yet slightly different  $\alpha$  textures were identified in previous studies on LFW joints of Ti-alloys mainly characterized by the prismatic plane being coplanar with the theoretical friction plane and the  $\langle 11\bar{2}0 \rangle$  direction being parallel to the oscillation direction which was also the main material expulsion direction [40]–[42]. Furthermore a slight rotation in texture in the TMAZ was also observed in [41] compared to the weld center corroborating the results shown in this study. The differences between those and the  $\{0001\}\langle 11\bar{2}0 \rangle$  texture reported here with  $\langle 11\bar{2}0 \rangle$  parallel to the main expulsion direction, but perpendicular to the oscillation direction might be caused by: 1) the welding configuration (i.e. process parameters, aspect ratios of the welded blocks, the oscillating direction ...); 2) the experimental method chosen for texture identification (XRD, EBSD ...) and the area investigated which affects the fraction of NTMAZ incorporated in the analysis. Nevertheless it has been shown that the  $\{0001\}\langle 11\bar{2}0 \rangle$  texture of the  $\alpha/\alpha'$  phase revealed here resulted from the  $\{110\}\langle 111 \rangle$  texture of the  $\beta$  phase developing during LFW in the joint core. Similar texture of the  $\beta$  phase have been reported for LFW  $\beta$  Ti-alloys in [16], [43]; yet the authors are presently unable to explain the tendency of those precipitates towards developing specific variants rather than a random distribution among all the possible variants from the prior- $\beta$  grain with  $\{110\}\langle 111 \rangle$  orientations. This could be caused by concurrent developing residual stresses or temperature gradients during cooling. Furthermore, the proposal of an asymmetric texture development in the  $\beta$  phase towards different plastic behavior in the forging and the oscillating part (caused by forging and oscillating motion) stated in this study has not been reported in the literature yet, a preceding study

on LFW Ti17 also showed an asymmetric behavior between the forging and the oscillating part with the oscillating part being more affected by the heat flux [16].

### 3.5. POST-WELD HEAT TREATMENT

Previous studies [13], [42] highlighted the fact that LFW of Ti-alloys causes important residual stresses within the joint in the as-welded configuration which could be detrimental to the assembly fatigue resistance. It has been shown in [13] that ageing near- $\alpha$  Ti-alloy LFW joint at 700 °C permitted to lower the residual stresses drastically. However, authors in [11] identified that an ageing at 700 °C for 2 h led to a drop in toughness due to interface weakening resulting from  $\beta$  and silicide precipitation along the  $\alpha$  lath boundaries. Homogenizing PWHT through  $\beta$  annealing followed by  $\alpha+\beta$  ageing as realized in [16] has been tested by the authors, but led to a loss of the fully-equiaxed microstructure of the base material in favor of a lamellar microstructure (1000 °C/3 h ; 1000 °C  $\rightarrow$  400 °C at 2 °C/min). Such a microstructure was characterized by highly-textured  $\alpha$  macro-zones with significant hardness fluctuations ( $\alpha$  phase anisotropy) known to be detrimental to cold dwell fatigue resistance [2]. The PWHT shown here consisted in an  $\alpha+\beta$  annealing followed by ageing (910 °C/2 h ; 910 °C  $\rightarrow$  635 °C /2 h ; 635 °C/8 h) in order to allow the  $\alpha' \rightarrow \alpha+\beta$  decomposition and the  $\alpha$  globularization in the TMAZ to form a gradual microstructure refinement across the TMAZ.

OM and SEM observations on the joint after this PWHT are shown in Figure 21 depicting the local microstructure. The annealing in the  $\alpha+\beta$  domain at 80 K below the  $\beta$ -transus for 2 h permitted to decompose the  $\alpha'$  into equilibrium  $\alpha+\beta$  in the WL, in the

TMAZ this led to  $\alpha_s \rightarrow \beta$  transformation and partial  $\alpha \rightarrow \beta$  in the rest of the assembly without abnormal  $\beta$  grain growth due to grain pinning by remaining partially transformed  $\alpha_p$  nodules. Slow cooling followed by ageing at 635 °C allowed to form coarse entangled  $\alpha$  laths within a  $\beta$  matrix in the WL and equiaxed  $\alpha$  grains in the TMAZ. Furthermore no porosities/defects formerly present in the joint were noticeable after PWHT which might be due defect dissolution into the bulk as observed in diffusion bonding processes [44].

Figure 21 : Microstructure observations of the weld after PWHT with a) OM observation of the whole joint under polarized light; and SEM micrographs in BSE mode for b) the WL c) the TMAZ and d) the BM (unaffected by LFW but the PWHT). In the SEM images, the  $\alpha$  phase in dark grey is distinguishable from the  $\beta$  phase in light grey.

The effect of the PWHT on the microstructural features (i.e.  $\beta$  phase fraction,  $\alpha$  grain diameter/aspect ratio and micro-hardness) of the former LFW macro-zones and the base material are shown in Figure 22 in comparison with the ones of the base material as-received. It can be seen from these results that the PWHT ensured: 1) quasi-uniform levels of  $\beta$  phase fraction and micro-hardness were obtained in the whole assembly; 2) a gradual microstructure refinement from the HAZ to the WL instead of the as-welded sharp TMAZ/HAZ border; 3) microstructural features of the treated base material similar to the ones of the as-received configuration.

Figure 22 : Comparison of the microstructural features between the base material in the as-received configuration (BM AR) and the macro-zones of the joint after the PWHT depending on their distances to the weld center line. It revealed a gradual microstructure refinement in the joint core while exhibiting homogenized  $\beta$  phase fractions and hardness values across the weld. No significant changes were noted in the treated base material compared to the as-received configuration.

Complementary XRD investigations were performed on the joint and the base material after the PWHT, the diffractograms are shown in Figure 23. Similar results were obtained between the base material after the PWHT and in the as-received configuration corroborating the microstructural observations. The surprisingly high intensity of the  $(11\bar{2}0)$  peak in the joint indicates that a strong texture is remaining in the weld after the PWHT. The 0001 and  $11\bar{2}0$  pole figures of the  $\alpha$  orientations in the WL shown in Figure 24 confirmed that a weakened  $\{0001\}\langle 11\bar{2}0\rangle$  is still present after PWHT. A  $\langle 11\bar{2}0\rangle$  pole close to the  $\langle y\rangle$  axis corroborates the texture observed by XRD. The residual  $\beta$  matrix formed by the PWHT from the martensitic microstructure also showed a significant  $\{110\}\langle 111\rangle$  texture resembling the one identified through the reconstruction of the  $\beta$  grains in Figure 17. No particular texture was noticeable any longer past the former NTMAZ border after PWHT.

Figure 23 : XRD diffractograms of restricted ranges of the diffraction angle of both heat treated joint and base material (BM) confirming the  $\alpha' \rightarrow \alpha + \beta$  decomposition in the joint and the presence of a strong texture in the  $\alpha$  phase. The surface irradiated is  $\{xz\}$ .

Figure 24 : a) 0001 and  $11\bar{2}0$  pole figures of the  $\alpha$  phase b) 110 and 111 pole figures of the  $\beta$  phase in the acicular central band after PWHT showing weakened  $\{0001\}\langle 11\bar{2}0\rangle$  and  $\{110\}\langle 111\rangle$  textures compared to the as-welded WL.

#### 4. CONCLUSION

A sound weld has been achieved by LFW on the near- $\alpha$  alloy Ti6242. The microstructures and hardness properties resulting from the process have been investigated in the as-welded condition as well as after a PWHT and the following conclusions can be drawn:

- 1) The supra-transus thermo-mechanical loads occurring near the contact interface caused the formation of a hard joint characterized by three distinct zones: the WL made of highly textured ultra-fine martensitic  $\alpha'$  laths precipitated within fine recrystallized prior- $\beta$  grains, the TMAZ consisting of highly deformed  $\alpha_p$  nodules and  $\alpha_s$  fragments with scattered retained  $\beta$  phase, and the HAZ indistinguishable from the base material but displaying a slight increase in hardness which might be due to residual stresses.
- 2) The high strain and strain rates combined with supra-transus temperatures activated recrystallization and recovery mechanisms to accommodate the deformation. Prior- $\beta$  grain reconstruction permitted to identify three main  $\beta$  texture components formed before cooling depending on the local asymmetrical deformation conditions. All three components have their  $\langle 111\rangle$  directions aligned with  $\langle x\rangle$  (perpendicular to the oscillation axis), the  $\langle 110\rangle$  direction is aligned with  $\langle z\rangle$  and  $\langle y\rangle$  for the forging and the oscillating NTMAZs respectively; a twin-symmetric component was formed in large clusters in the joint core. Martensitic  $\beta \rightarrow \alpha'$  (WL and NTMAZ) and  $\beta_T \rightarrow \alpha_s$

(FTMAZ) transformations upon cooling resulted in a strong texture in the core of the joint with the {0001} plane being parallel with the friction plane {xy} and the  $\langle 11\bar{2}0 \rangle$  direction being aligned with the transversal direction  $\langle x \rangle$ .

- 3) The material consumption and the temperature fields revealed a rather symmetrical behavior between the oscillating and the forging block.
- 4) A PWHT is proposed which homogenizes the hardness properties within the whole assembly by  $\alpha'$  decomposition into equilibrium  $\alpha+\beta$  acicular microstructure in the WL and  $\alpha$  globularization in the TMAZ ensuring smooth microstructure transitions across the joint.

## **ACKNOWLEDGEMENT**

The authors acknowledge the financial support from the French National Research Agency (ANR) through the OPTIMUM ANR-14-CE27-0017 project as well as the Spatial and Aeronautic Research Foundation, the Hauts-de-France Region and the European Regional Development Fund (ERDF) 2014/2020 for the funding of this work. The authors are also grateful to ACB for providing LFW welded samples and Airbus for both their technical support.

## **DATA AVAILABILITY**

The raw/processed data required to reproduce these findings can be shared on request.

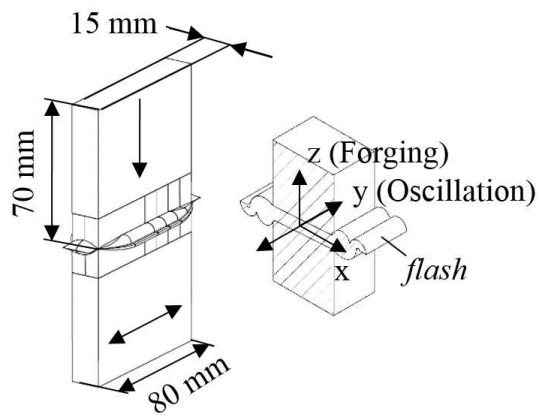
## REFERENCES

- [1] R. Boyer, G. Welsch, and E. W. Collings, Eds., *Materials properties handbook: titanium alloys*, 4. printing. Materials Park, Ohio: ASM International, 2007.
- [2] G. Lütjering and J. C. Williams, *Titanium*. Berlin, Heidelberg: Springer Berlin Heidelberg, 2003.
- [3] J. L. Huang, N. Warnken, J.-C. Gebelin, M. Strangwood, and R. C. Reed, "On the mechanism of porosity formation during welding of titanium alloys," *Acta Mater.*, vol. 60, no. 6–7, pp. 3215–3225, Apr. 2012.
- [4] M. J. J. Donachie, *Titanium A Technical Guide Second Edition*. 2000.
- [5] Z. Liu and G. Welsch, "Effects of oxygen and heat treatment on the mechanical properties of alpha and beta titanium alloys," *Metall. Trans. A*, vol. 19, no. 3, pp. 527–542, 1988.
- [6] T. Ando, K. Nakashima, T. Tsuchiyama, and S. Takaki, "Microstructure and mechanical properties of a high nitrogen titanium alloy," *Mater. Sci. Eng. A*, vol. 486, no. 1–2, pp. 228–234, Jul. 2008.
- [7] A. R. McAndrew, P. A. Colegrove, A. C. Addison, B. C. D. Flipo, M. J. Russell, and L. A. Lee, "Modelling of the workpiece geometry effects on Ti-6Al-4V linear friction welds," *Mater. Des.*, vol. 87, pp. 1087–1099, Dec. 2015.
- [8] A. Vairis and M. Frost, "High frequency linear friction welding of a titanium alloy," *Wear*, vol. 217, pp. 117–131, 1998.
- [9] P. Wanjara and M. Jahazi, "Linear friction welding of Ti-6Al-4V: processing, microstructure, and mechanical-property inter-relationships," *Metall. Mater. Trans. A*, vol. 36, no. 8, pp. 2149–2164, 2005.
- [10] W. A. Baeslack, "Characterization of Solid-Phase Welds Between Ti-6Al-2Sn-4Zr-2Mo-0.1Si and Ti-13.5Al-21.5Nb Titanium Aluminide," *Mater. Charact.*, vol. 33, pp. 357–367, 1994.
- [11] S. D. Meshram and T. Mohandas, "Influence of matrix microstructure on aging response of near alpha titanium alloy (IMI834) parent metal and welds on toughness," *Mater. Sci. Technol.*, vol. 27, no. 1, pp. 235–239, Jan. 2011.
- [12] E. Dalgaard, P. Wanjara, J. Gholipour, and J. J. Jonas, "Linear Friction Welding of a Forged Near- $\alpha$  Titanium Alloy," *Mater. Sci. Forum*, vol. 706–709, pp. 211–216, Jan. 2012.
- [13] P. Frankel, M. Preuss, A. Steuwer, P. J. Withers, and S. Bray, "Comparison of residual stresses in Ti-6Al-4V and Ti-6Al-2Sn-4Zr-2Mo linear friction welds," *Mater. Sci. Technol.*, vol. 25, no. 5, pp. 640–650, May 2009.
- [14] W. Li, A. Vairis, M. Preuss, and T. Ma, "Linear and rotary friction welding review," *Int. Mater. Rev.*, vol. 61, no. 2, pp. 71–100, Feb. 2016.
- [15] A. R. McAndrew, P. A. Colegrove, C. Bühr, B. C. D. Flipo, and A. Vairis, "A literature review of Ti-6Al-4V linear friction welding," *Prog. Mater. Sci.*, vol. 92, pp. 225–257, Mar. 2018.
- [16] D. Ballat-Durand, S. Bouvier, M. Risbet, and W. Pantleon, "Multi-scale and multi-technic microstructure analysis of a linear friction weld of the metastable- $\beta$  titanium alloy Ti-5Al-2Sn-2Zr-4Mo-4Cr (Ti17) towards a new Post-Weld Heat Treatment," *Mater. Charact.*, vol. 144, pp. 661–670, Oct. 2018.

- [17] J. M. Garcia and T. F. Morgeneyer, "Strength and fatigue strength of a similar Ti-6Al-2Sn-4Zr-2Mo-0.1Si linear friction welded joint," *Fatigue & Fracture of Engineering Materials & Structures*. To be published
- [18] ASM International, Ed., *Metallography and microstructures*, New ed. Metals Park, Ohio: American Society for Metals, 2004.
- [19] D. Banerjee and J. C. Williams, "Perspectives on Titanium Science and Technology," *Acta Mater.*, vol. 61, no. 3, pp. 844–879, Feb. 2013.
- [20] S. L. Semiatin, T. M. Lehner, J. D. Miller, R. D. Doherty, and D. U. Furrer, "Alpha/Beta Heat Treatment of a Titanium Alloy with a Nonuniform Microstructure," *Metall. Mater. Trans. A*, vol. 38, no. 4, pp. 910–921, Jun. 2007.
- [21] S. Malinov, W. Sha, Z. Guo, C. . Tang, and A. . Long, "Synchrotron X-ray diffraction study of the phase transformations in titanium alloys," *Mater. Charact.*, vol. 48, no. 4, pp. 279–295, Jun. 2002.
- [22] G. D. Wen *et al.*, "Mathematical modelling of joint temperature during linear friction welding of dissimilar Ti-6.5 Al-3.5 Mo-1.5 Zr-0.3 Si and Ti-5Al-2Sn-2Zr-4Mo-4Cr alloys," *J Eng Sci Technol Rev*, vol. 5, no. 3, pp. 35–38, 2012.
- [23] C. Owen, S. Jeffs, K. Perkins, and S. Bray, "The evolution of Ti-6Al-4V following extreme thermo-mechanical processing," in *Proc. 16th World Conference on Titanium*, 2016, pp. 455–460.
- [24] J. W. Elmer, T. A. Palmer, S. S. Babu, W. Zhang, and T. DebRoy, "Phase transformation dynamics during welding of Ti-6Al-4V," *J. Appl. Phys.*, vol. 95, no. 12, pp. 8327–8339, Jun. 2004.
- [25] A. Idhil Ismail, M. Dehmas, E. Aeby-Gautier, and B. Appolaire, "In-situ investigation of phase transformation kinetics in Ti-6Al-4V under rapid heating condition using high-energy synchrotron diffraction," *Proc. 13th World Conf. Titan.*, 2016.
- [26] S. C. Wang, M. Aindow, and M. J. Starink, "Effect of self-accommodation on  $\alpha/\alpha$  boundary populations in pure titanium," *Acta Mater.*, vol. 51, no. 9, pp. 2485–2503, May 2003.
- [27] V. Tari, A. D. Rollett, and H. Beladi, "Back calculation of parent austenite orientation using a clustering approach," *J. Appl. Crystallogr.*, vol. 46, no. 1, pp. 210–215, Feb. 2013.
- [28] M. G. Glavicic, P. A. Kobryn, T. R. Bieler, and S. L. Semiatin, "A method to determine the orientation of the high-temperature beta phase from measured EBSD data for the low-temperature alpha phase in Ti-6Al-4V," *Mater. Sci. Eng. A*, vol. 346, no. 1–2, pp. 50–59, Apr. 2003.
- [29] L. Germain, S. R. Dey, M. Humbert, and N. Gey, "Determination of parent orientation maps in advanced titanium-based alloys," *J. Microsc.*, vol. 227, no. 3, pp. 284–291, Sep. 2007.
- [30] L. Germain, N. Gey, and M. Humbert, "Reliability of reconstructed  $\beta$ -orientation maps in titanium alloys," *Ultramicroscopy*, vol. 107, no. 12, pp. 1129–1135, Nov. 2007.
- [31] B. K. K., K. K. Saxena, S. R. Dey, V. Pancholi, and A. Bhattacharjee, "Processing map-microstructure evolution correlation of hot compressed near alpha titanium alloy (TiHy 600)," *J. Alloys Compd.*, vol. 691, pp. 906–913, Jan. 2017.
- [32] X. Fan, Q. Li, A. Zhao, Y. Shi, and W. Mei, "The Effect of Initial Structure on Phase Transformation in Continuous Heating of a TA15 Titanium Alloy," *Metals*, vol. 7, no. 6, p. 200, Jun. 2017.

- [33] P. Homporova, C. Poletti, M. Stockinger, and F. Warchomicka, "Dynamic phase evolution in titanium alloy Ti-6Al-4V," in *Proc. 12th World Conference on Titanium*, 2011, pp. 19–42.
- [34] I. Balasundar, T. Raghu, and B. P. Kashyap, "Modeling the hot working behavior of near- $\alpha$  titanium alloy IMI 834," *Prog. Nat. Sci. Mater. Int.*, vol. 23, no. 6, pp. 598–607, Dec. 2013.
- [35] R. Sedlacek, W. Blum, J. Kratochvil, and S. Forest, "Subgrain Formation during Deformation: Physical Origin and Consequences," *Metall. Mater. Trans. A*, vol. 32A, 2001.
- [36] T. Sakai and J. J. Jonas, "Overview no. 35 dynamic recrystallization: mechanical and microstructural considerations," *Acta Metall.*, vol. 32, no. 2, pp. 189–209, 1984.
- [37] C. Perdrix, M. Y. Perrin, and F. Montheillet, "Comportement mecanique et evolution structurale de l'aluminium au cours d'une deformation a chaud de grande amplitude," *Mem Sci Rev Métal*, vol. 78, pp. 309–320, 1981.
- [38] D. A. Hughes and N. Hansen, "High angle boundaries formed by grain subdivision mechanisms," *Acta Mater.*, vol. 45, no. 9, pp. 3871–3886, 1997.
- [39] W. Pantleon, "Deformation structure versus grain structure after severe plastic deformation," *Probl. Mater. Sci.*, vol. 52, pp. 13–23, 2007.
- [40] M. M. Attallah, M. Preuss, and S. Bray, "Microstructural development during linear friction welding of titanium alloys," *Trends Weld. Res. 2008*, pp. 486–491, 2009.
- [41] M. Karadge, M. Preuss, C. Lovell, P. J. Withers, and S. Bray, "Texture development in Ti–6Al–4V linear friction welds," *Mater. Sci. Eng. A*, vol. 459, no. 1–2, pp. 182–191, Jun. 2007.
- [42] J. Romero, M. M. Attallah, M. Preuss, M. Karadge, and S. E. Bray, "Effect of the forging pressure on the microstructure and residual stress development in Ti–6Al–4V linear friction welds," *Acta Mater.*, vol. 57, no. 18, pp. 5582–5592, Oct. 2009.
- [43] E. Dalgaard, P. Wanjara, J. Gholipour, X. Cao, and J. J. Jonas, "Linear friction welding of a near- $\beta$  titanium alloy," *Acta Mater.*, vol. 60, no. 2, pp. 770–780, Jan. 2012.
- [44] N. F. Kazakov, Ed., *Diffusion Bonding of materials*. Oxford: Mir Publ, 1985.

a)



b)



Figure 1 : a) Sketch of the geometry of the welded parts and the sampling method for observations and diffraction analysis [16] with the forging direction  $\langle z \rangle$  and the oscillating direction  $\langle y \rangle$ ; b) picture of the whole assembly. The forging part is the upper part ( $z > 0$ ) and the oscillating part is the lower part ( $z < 0$ ).

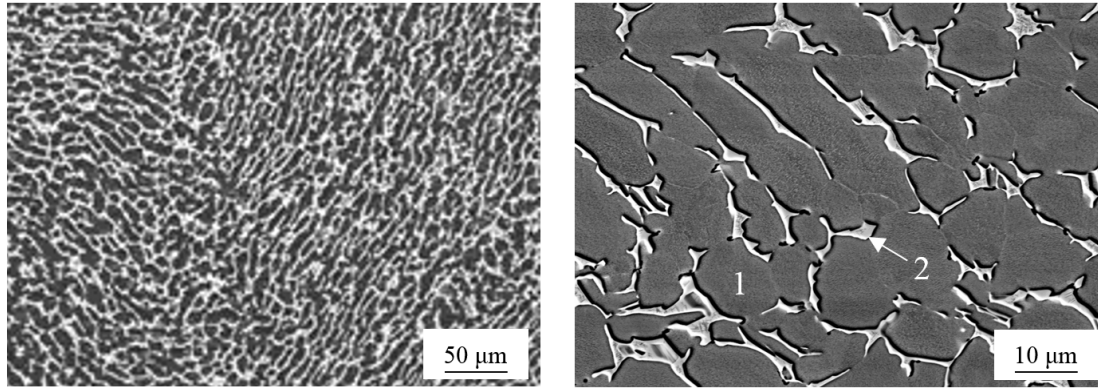


Figure 2 : Fully-equiaxed microstructure of the as-received Ti6242 base material. SEM micrographs of the  $\alpha_p$  nodules in dark grey (marker #1) within the bright  $\beta$  matrix (marker #2).

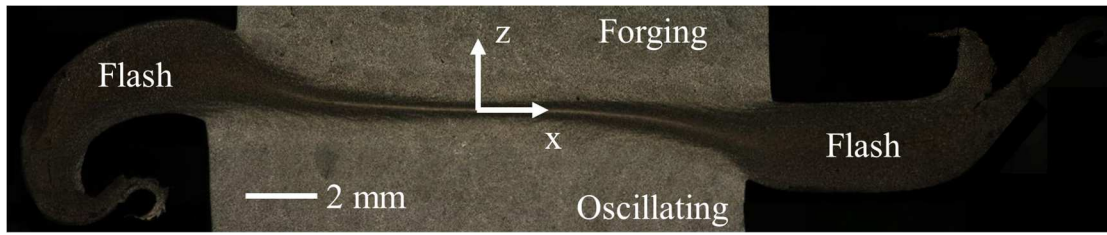


Figure 3 : Preliminary inspection of the weld by OM after etching revealing an offset in the alignment of the parts along  $x$ , asymmetrical flashes and the curvature of the joint.

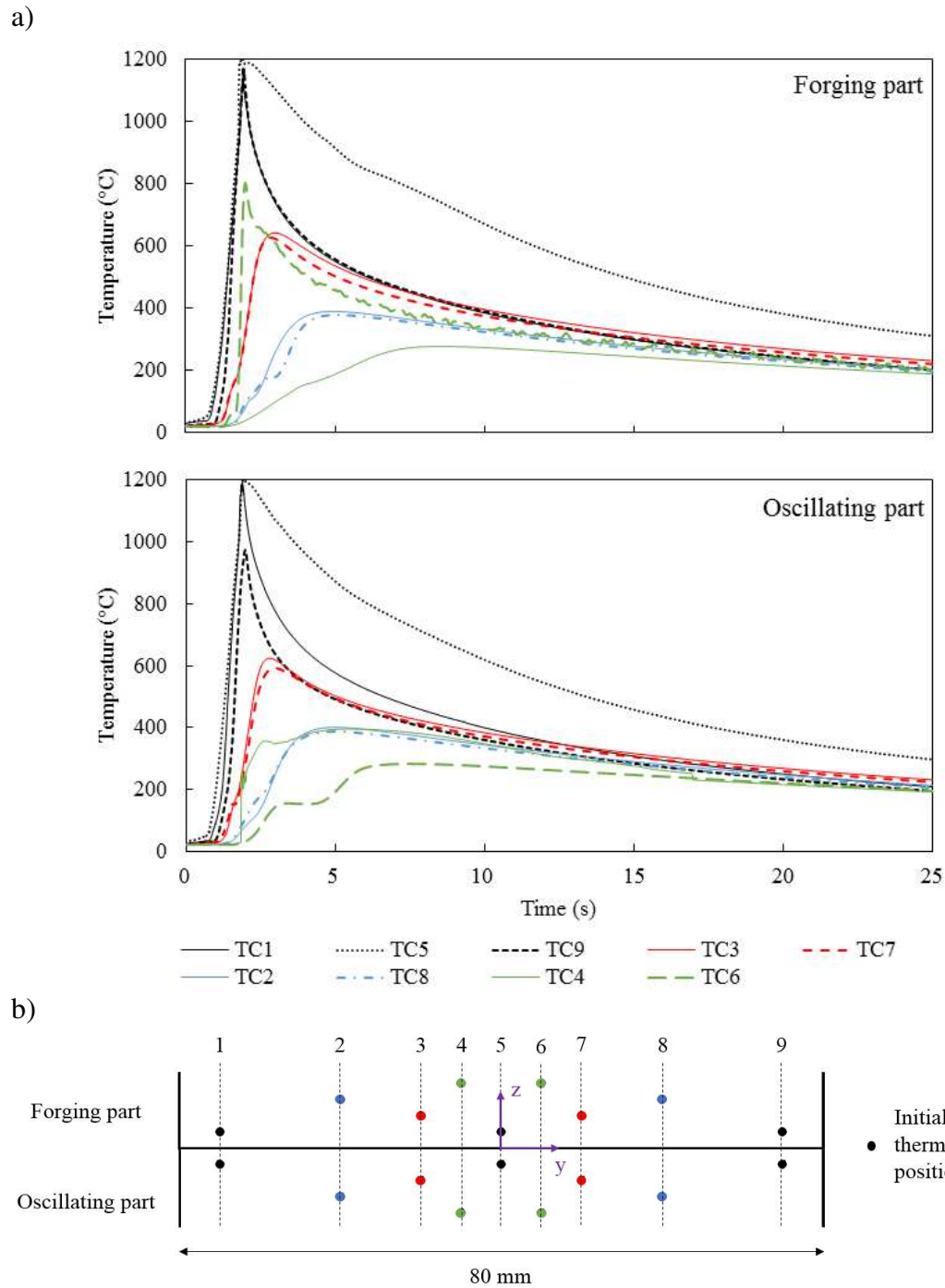


Figure 4 : Temperature measurements across the joint showing a) the thermocouple data from the forging part and the oscillating part; b) the initial thermocouple positions. The colors indicate the initial distance from the contact surface prior to axial shortening: TC1+5+9, TC3+7, TC2+8 and TC4+6 were placed at 2 mm, 4 mm, 6 mm and 8 mm, respectively.

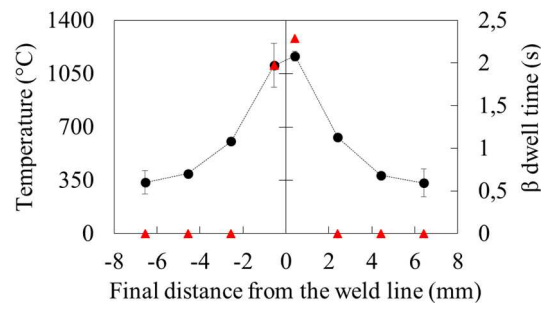


Figure 5 : Local temperature maxima measured by the thermocouples (black dots) in dependence on the final distance from the weld center line after axial shortening combined with the local dwell time in the  $\beta$  domain experienced during the process (red triangles).

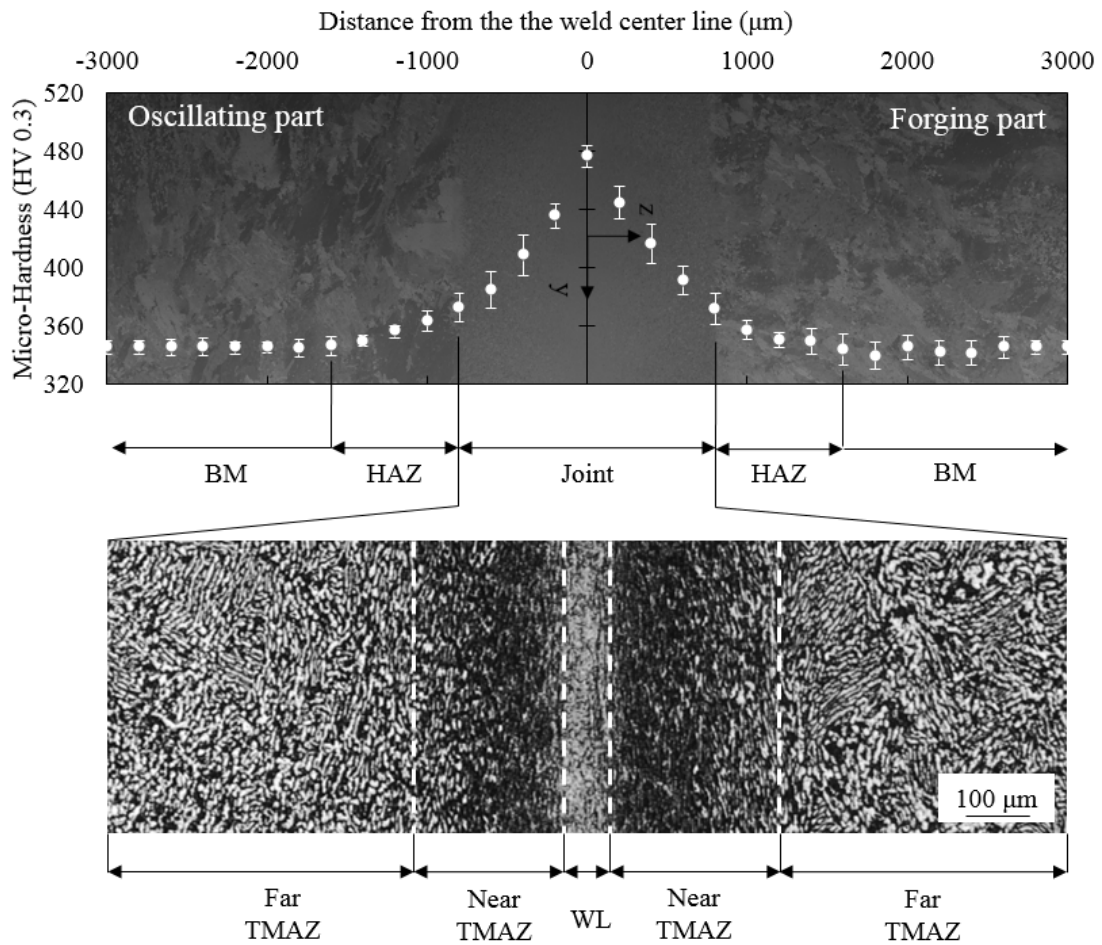
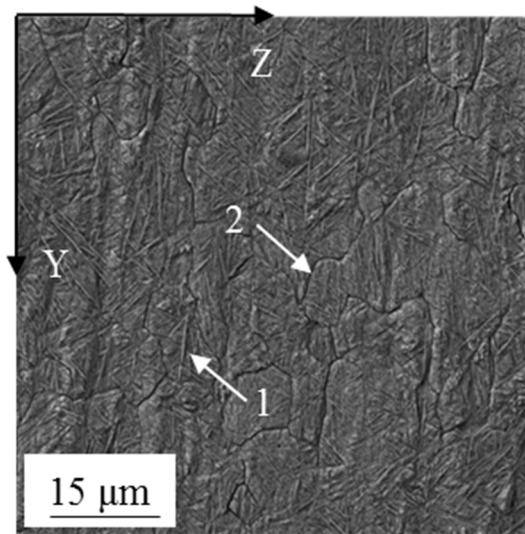
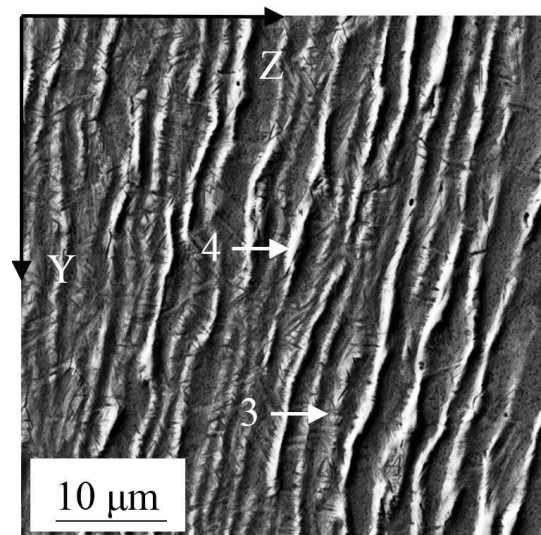


Figure 6 : Combined data from OM observations with polarized-light and corresponding local hardness across the Ti6242 LFW joint detailing the characteristic macro-zones: the Welding Line (WL), the Thermo-mechanically Affected Zone (TMAZ) and the Heat Affected Zone (HAZ). The polarized-light showed the global microstructure refinement in the joint and etching revealed a further subdivision of the TMAZ into the far-TMAZ (FTMAZ) just deformed, the near-TMAZ (NTMAZ) heavily deformed and the WL fully transformed.

a)



b)



c)

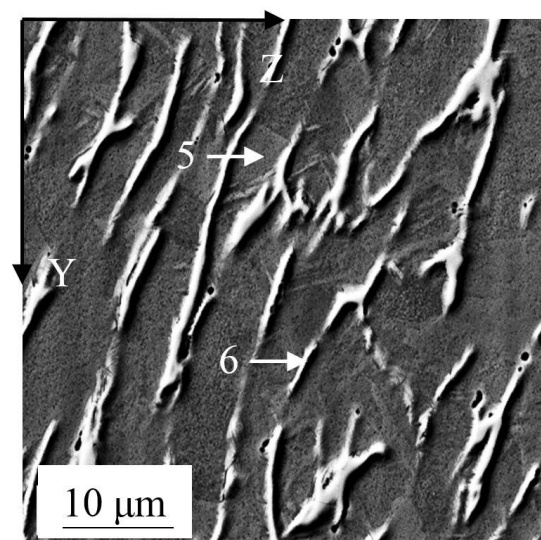


Figure 7 : Microscale observations by SEM in Back-Scatter Electron (BSE) mode of the joint showing the microstructures in the different zones within the joint a) WL: ultra-fine laths (1) precipitated within fine equiaxed grains (2); b) NTMAZ: highly deformed  $\alpha$  nodules (3) and transformed "Ghost" prior- $\beta$  matrix (4); c) FTMAZ: slightly deformed  $\alpha$  nodules with traces of fragmentation (5) and retained  $\beta$  matrix (6).

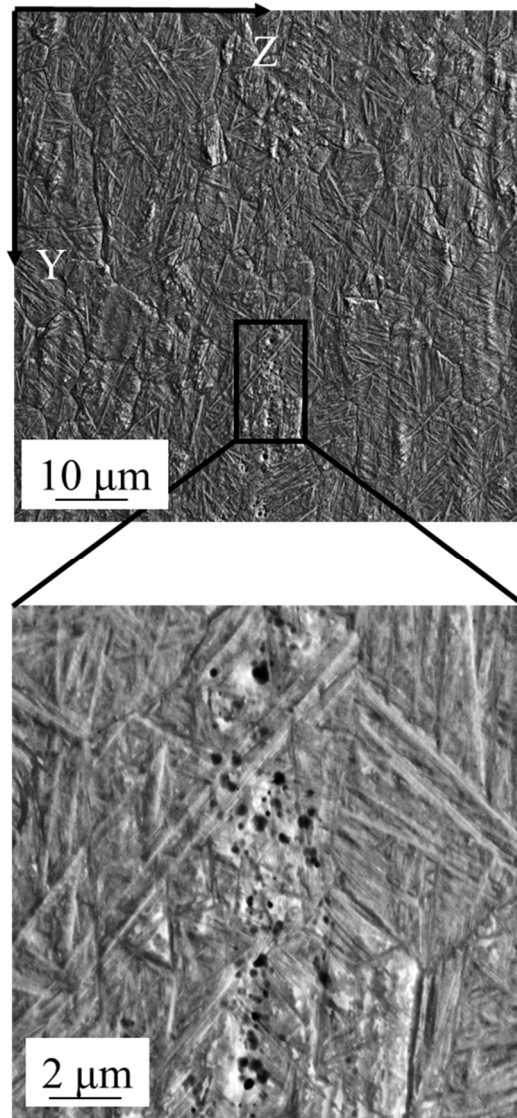


Figure 8 : Microscale observations by SEM in Back-Scatter Electron (BSE) mode of the center of the WL showing the presence of defects/porosities along the central line.

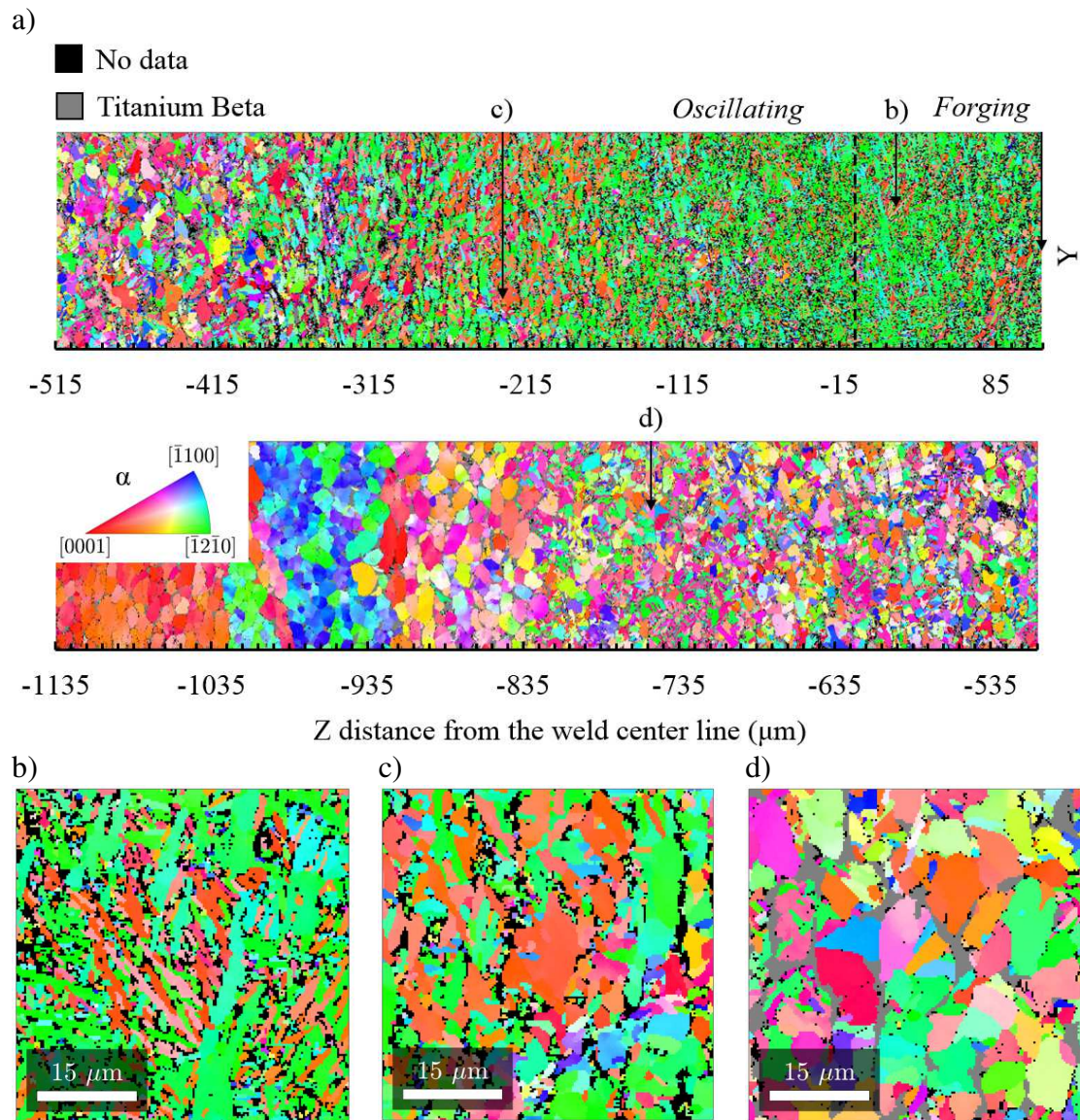


Figure 9 : EBSD orientation map of the HCP phase (step size=0.3  $\mu\text{m}$ ) within the joint highlighting a) the microstructure refinement at the TMAZ/HAZ border ( $z \approx 800 \mu\text{m}$ ) and the change of microstructure in the joint from fragmented-like in the TMAZ to acicular in the WL. The arrows indicate the positions of the three magnified local regions b) WL HCP entangled laths; c) NTMAZ squeezed/shrunk prior-nodular  $\alpha$  and fine laths; d) FTMAZ showing fragmented-like coarse prior-nodular  $\alpha$  within a  $\beta$  matrix (grey). The colors indicate the crystallographic directions of the HCP phase along the  $\langle x \rangle$  direction. Grains formed by less than five measurement points were considered as not indexed.

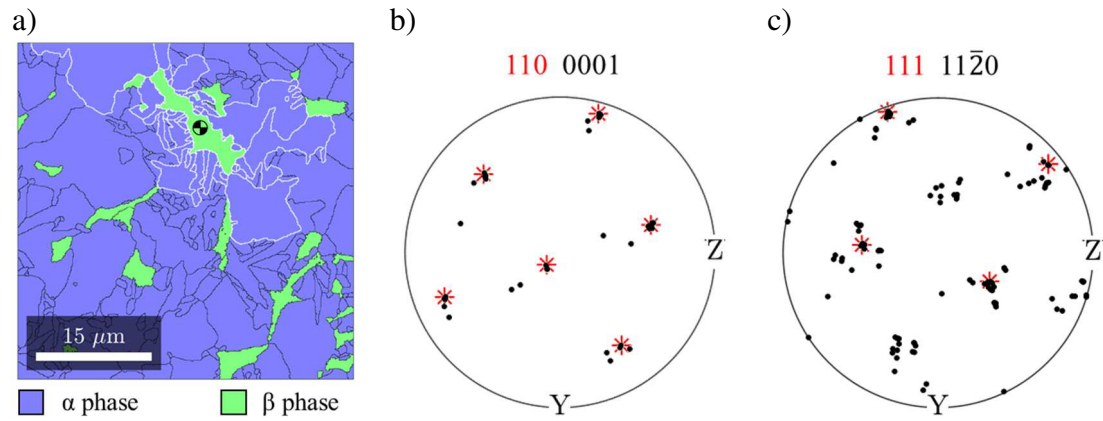


Figure 10 : EBSD analysis in the FTMAZ highlighting of the Burgers Orientation Relationship ( $\{0001\}_\alpha // \{110\}_\beta$  ;  $\langle 11\bar{2}0 \rangle_\alpha // \langle 111 \rangle_\beta$ ) between the  $\beta$  matrix (green) and neighboring  $\alpha$  fragments (blue) showing in a) a selected  $\beta$  grain marked by the symbol and its neighbors (outlined by white boundaries); b)-c) overlaid 110-0001 and 111-11 $\bar{2}$ 0 pole figures of the mean grain orientations of the reference  $\beta$  grain (red stars) and its  $\alpha$  neighbors (black dots).

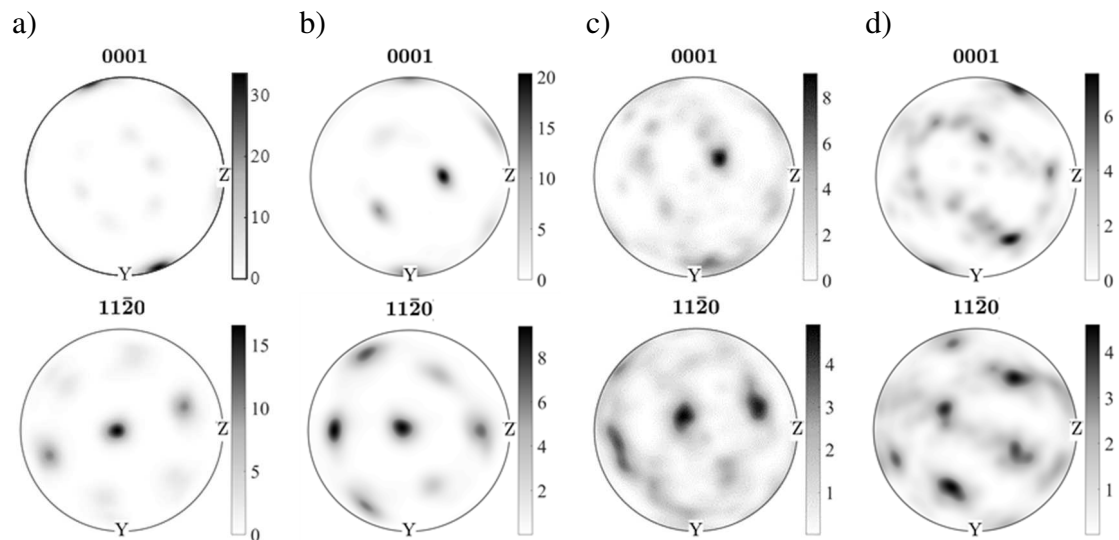


Figure 11 : Local texture analysis of the HCP phase from the orientation map in Figure 9 through 0001 and  $11\bar{2}0$  pole figures obtained from: a)  $z = [50 ; -50] \mu\text{m}$  (WL); b)  $z = [-150 ; -250] \mu\text{m}$  (oscillating NTMAZ); c)  $z = [-350 ; -450] \mu\text{m}$  (oscillating FTMAZ); d)  $z = [-550 ; -650] \mu\text{m}$  (oscillating FTMAZ). An orientation density function was obtained from the measured orientations using a half width of  $2^\circ$  and used to plot the pole figures with a minimum of 120 000 orientations (10000 and 3000 grains in the WL and in the TMAZ, respectively).

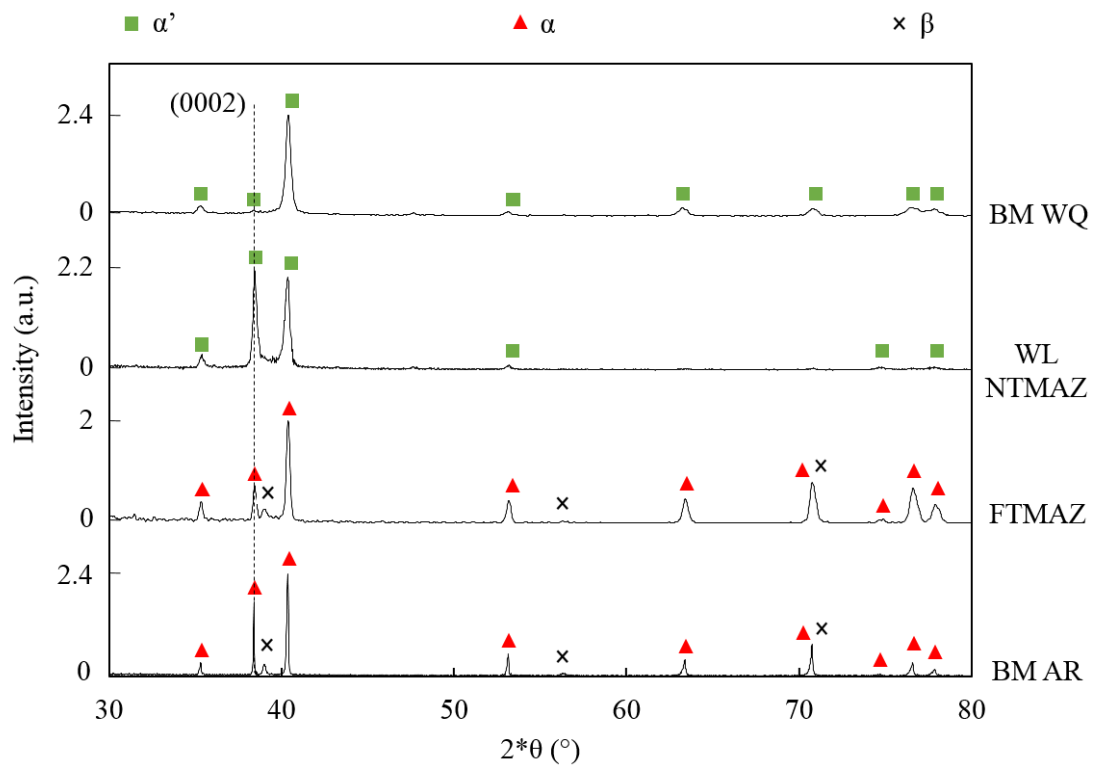


Figure 12 : XRD diffractograms of restricted ranges of the diffraction angle of the core of the joint (WL+NTMAZs) and the FTMAZ compared to the base material water-quenched (BM WQ) sample and the base material as-received (BM AR). The surface irradiated is {yz}.

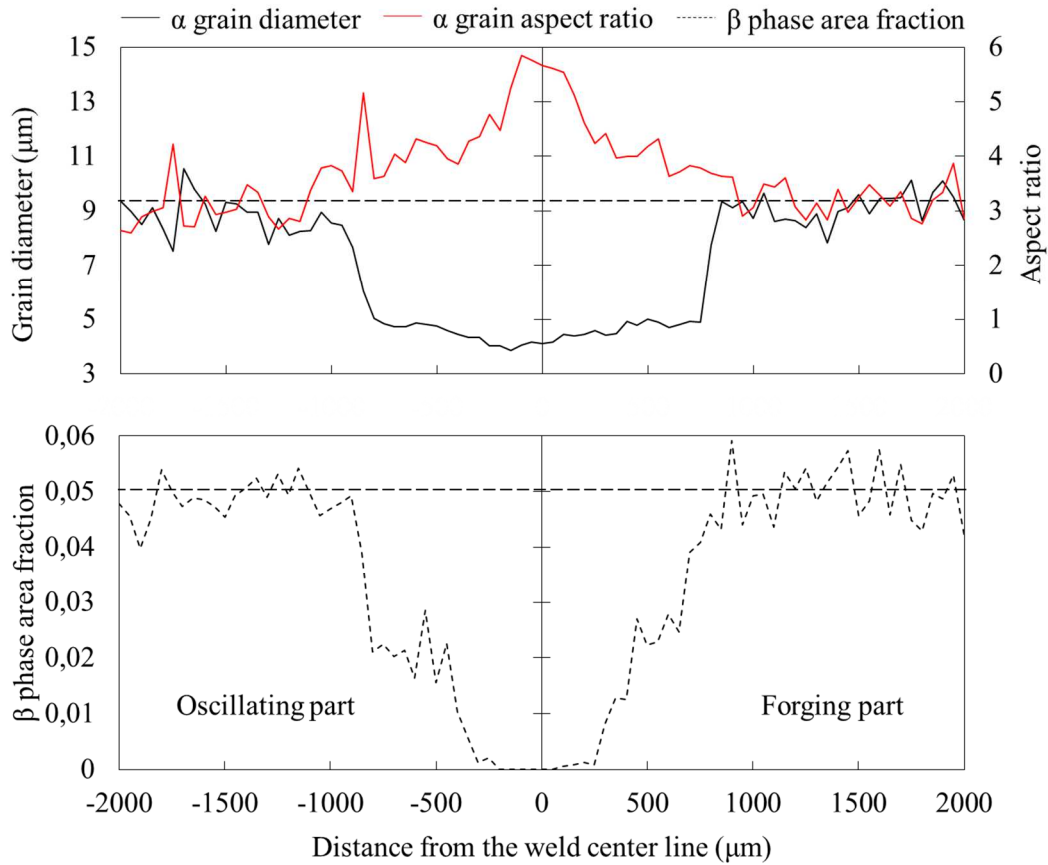


Figure 13 : Evolution of the  $\alpha/\alpha'$  grain diameter (longest distance between any two pixels along the grain boundary) and aspect ratio (length/width) combined with the local  $\beta$  phase area fraction across the joint (along  $\langle z \rangle$ ) showing an abrupt microstructural refinement at the TMAZ/HAZ border, a gradual loss of  $\beta$  phase in the FTMAZ and its total absence in the WL and the NTMAZ.

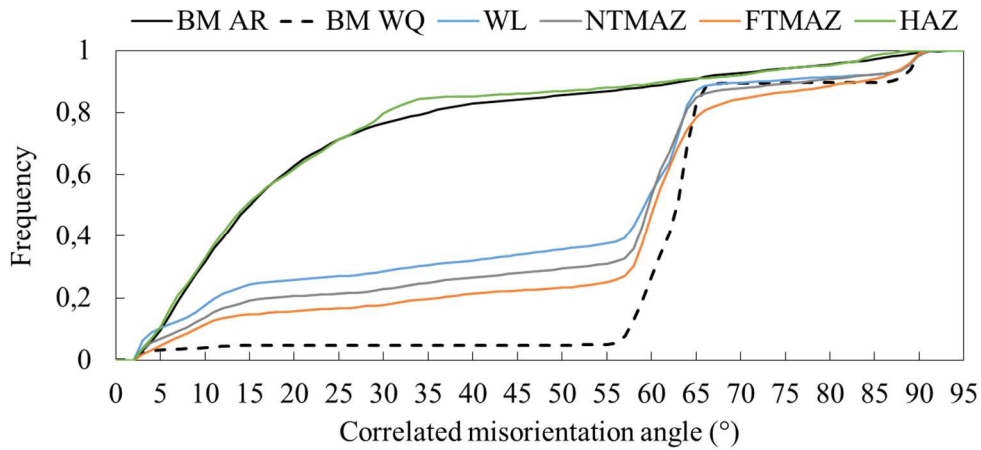


Figure 14 : Cumulated correlated misorientation angle distributions across the boundaries between  $\alpha/\alpha'$  grains in the different joint zones compared to the base material as-received (BM AR) and the water-quenched sample (BM WQ). The kinks at  $60^\circ$  and  $90^\circ$  are typically observed between  $\alpha$  variants precipitated from a common  $\beta$  parent orientation. The zones investigated were taken from the orientation data in Figure 9 from the oscillating part at the following  $\langle z \rangle$  positions in  $\mu\text{m}$ : [50 ; -50], [-150 ; -250], [-550 ; -650] and [-950 ; -1050] for the WL, NTMAZ, FTMAZ and the HAZ, respectively. A threshold of  $2^\circ$  was used for grain boundary detection. The data of the water-quenched sample were obtained from 4780  $\alpha'$  laths precipitated within the same prior- $\beta$  parent grain. The data of the base material as-received were obtained from 2210  $\alpha_p$  nodules from a single  $4.10^3 \mu\text{m}^2$  macro-zone.

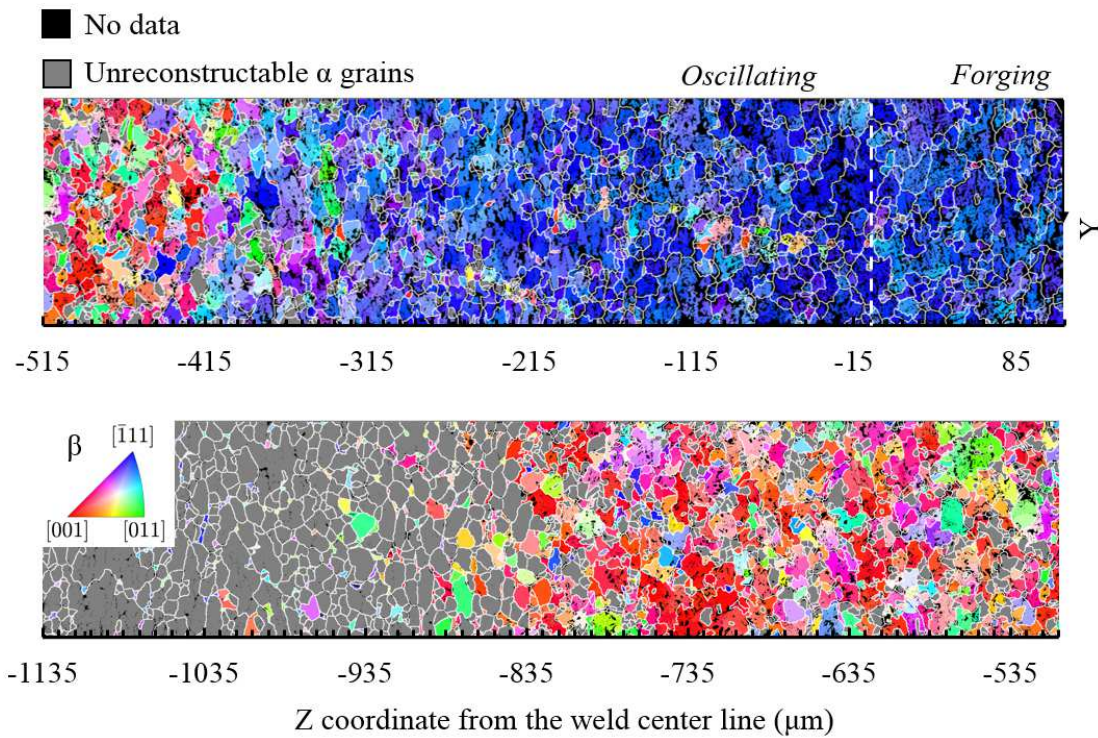


Figure 15 : Orientation map of the BCC  $\beta$  phase obtained by parent grain reconstruction from the  $\alpha/\alpha'$  clusters shown in Figure 9 combined with the experimental retained  $\beta$  matrix displaying: the significant area fraction of  $\alpha$  “fragments” sharing common  $\beta$  parents in the TMAZ associated with a gradual  $\beta$   $\langle 111 \rangle$  texture development in the NTMAZ and a noticeable prior- $\beta$  grain fragmentation in the WL. The color indicates the crystallographic directions of the BCC  $\beta$  phase along the  $\langle x \rangle$  direction. The white lines represent grain boundaries with a misorientation angle above of  $5^\circ$ . The grey color indicates unreconstructable fragments.

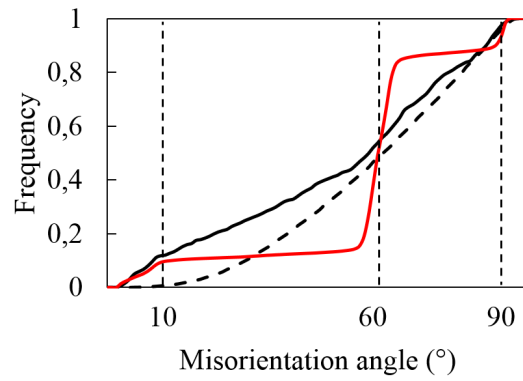


Figure 16 : Cumulated correlated misorientation angle distributions excluding the reconstructable fragments (solid red) from the unreconstructable ones (solid black) compared to uncorrelated distribution of random orientations (dashed black). 650 unreconstructable  $\alpha$  grains were used in the analysis.

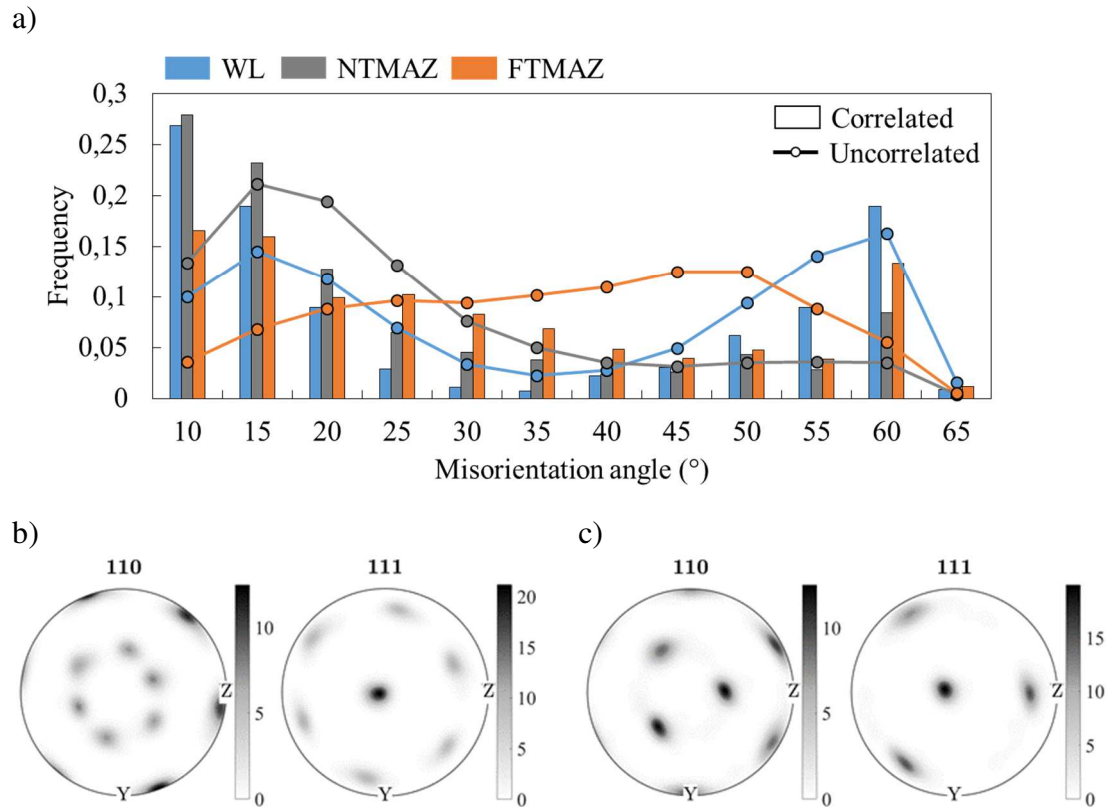


Figure 17 : a) Correlated misorientation angle distributions across the boundaries of the reconstructed prior- $\beta$  grains and the corresponding uncorrelated misorientation angle distributions in the WL, the oscillating NTMAZ and the oscillating FTMAZ; recalculated 110 and 111 pole figures of the reconstructed prior- $\beta$  grains in b) the WL and c) the oscillating NTMAZ. With decreasing distance from the weld center, i.e. from the FTMAZ to the WL, first an increase in the frequency of low misorientation angles at the expense of higher misorientation angles is observed, followed by a slight decrease in favor of boundaries with very high angles. These high fraction of boundaries with very high angles are a consequence of the developing texture from one dominating component towards two dominating components. A threshold of  $5^\circ$  was used for grain boundary detection and halfwidth of  $5^\circ$  was set for the orientation distribution function calculation.

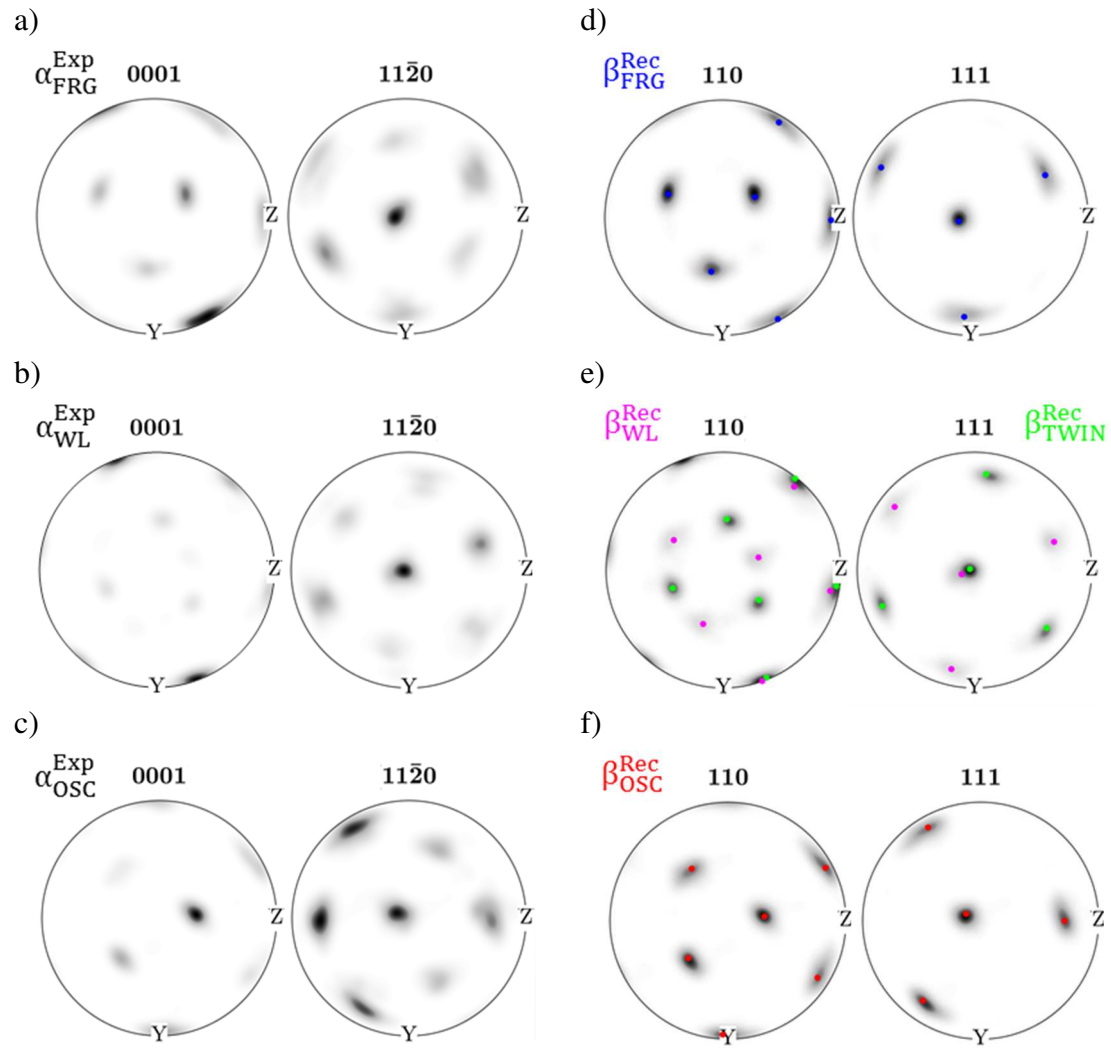


Figure 18 : Local analysis of the BCC <111> texture development among the prior- $\beta$  grains close to the weld center line relying on the  $\beta$  reconstructed orientations ( $\beta^{\text{Rec}}$ ) from the experimental  $\alpha/\alpha'$  orientations ( $\alpha^{\text{Exp}}$ ). The 0001 and  $11\bar{2}0$  pole figures of the  $\alpha^{\text{Exp}}$  are plotted for a) the forging NTMAZ ( $\alpha_{\text{FRG}}$ ); b) the WL ( $\alpha_{\text{WL}}$ ) and c) the oscillating NTMAZ ( $\alpha_{\text{OSC}}$ ). The corresponding 110 and 111 pole figures of the  $\beta^{\text{Rec}}$  are plotted in d)-e). Four ideal orientations are marked, one for each of the NTMAZ ( $\beta_{\text{FRG}}$  on the forging side in blue and  $\beta_{\text{OSC}}$  on the oscillating side in red) and two in the WL (a local component  $\beta_{\text{WL}}$  in purple and the corresponding twin component  $\beta_{\text{TWIN}}$  in green).

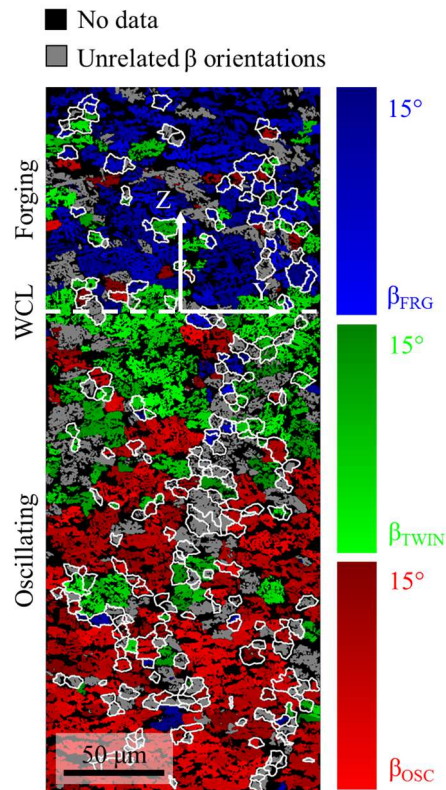


Figure 19 : Spatial distribution of the three main  $\{hkl\}\langle 111 \rangle$  texture components of the  $\beta$  phase (i.e.  $\beta_{FRG}$ ,  $\beta_{OSC}$ , and  $\beta_{TWIN}$ ) combined with the local angular deviation from the closest reference orientation. The recrystallized nuclei highlighted by white boundaries were identified as having at least one boundary with a misorientation above  $15^\circ$  and ensuring a grain orientation spread lower than  $1^\circ$ . The white dashed line represents the weld center line (WCL).

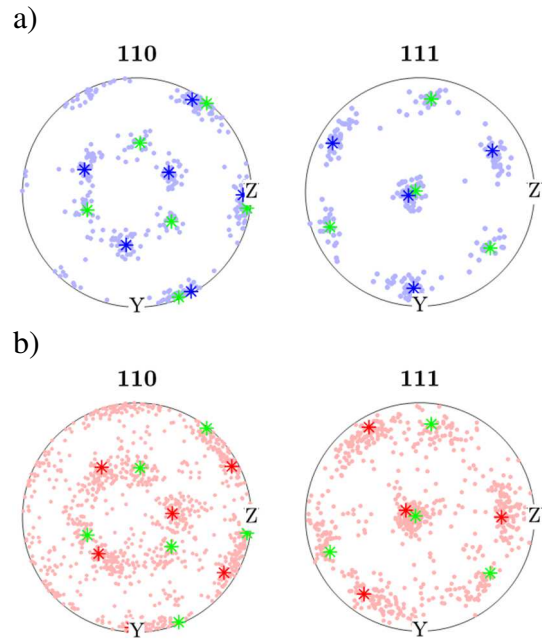


Figure 20 : 110 and 111 pole figures of the mean orientation of all recrystallized nuclei for a) the forging part and b) the oscillating part. The ideal orientations  $\beta_{FRG}$ ,  $\beta_{OSC}$  and  $\beta_{TWIN}$  are shown in blue, red and green stars respectively.

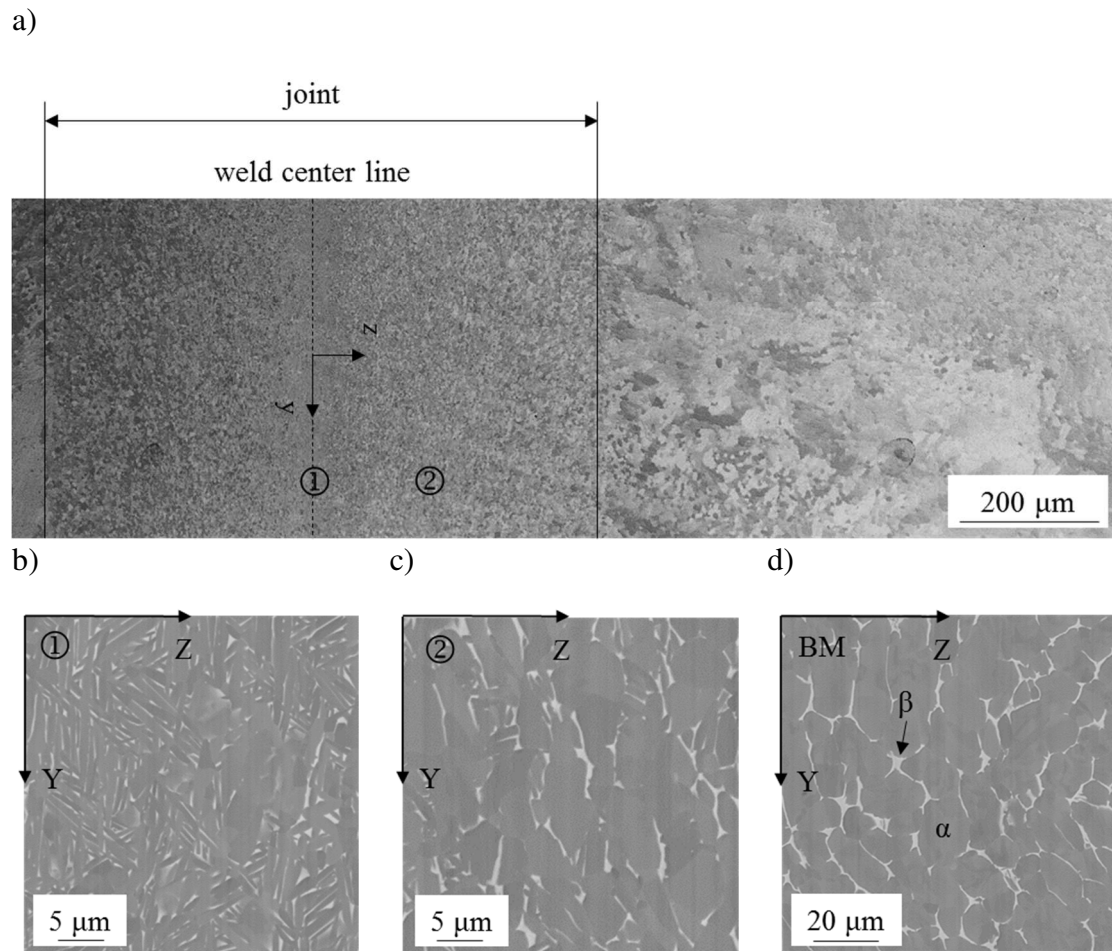


Figure 21 : Microstructure observations of the weld after PWHT with a) OM observation of the whole joint under polarized light; and SEM micrographs in BSE mode for b) the WL c) the TMAZ and d) the BM (unaffected by LFW but the PWHT). In the SEM images, the  $\alpha$  phase in dark grey is distinguishable from the  $\beta$  phase in light grey.

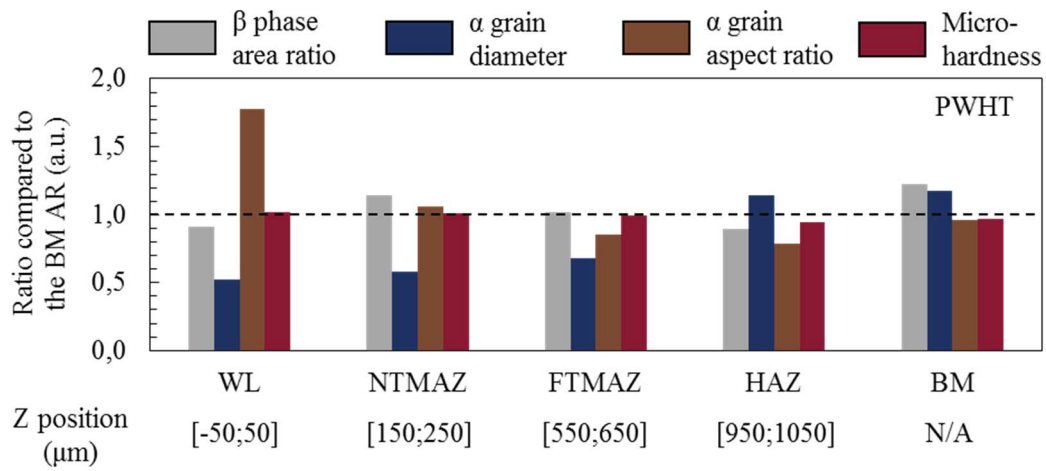


Figure 22 : Comparison of the microstructural features between the base material in the as-received configuration (BM AR) and the macro-zones of the joint after the PWHT depending on their distances to the weld center line. It revealed a gradual microstructure refinement in the joint core while exhibiting homogenized  $\beta$  phase fractions and hardness values across the weld. No significant changes were noted in the treated base material compared to the as-received configuration.

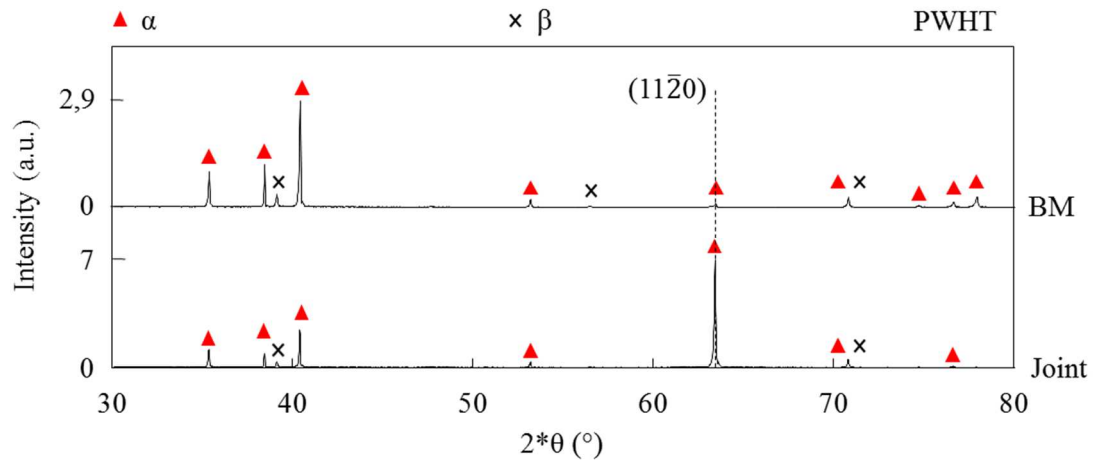


Figure 23 : XRD diffractograms of restricted ranges of the diffraction angle of both heat treated joint and base material (BM) confirming the  $\alpha' \rightarrow \alpha + \beta$  decomposition in the joint and the presence of a strong texture in the  $\alpha$  phase. The surface irradiated is  $\{xz\}$ .

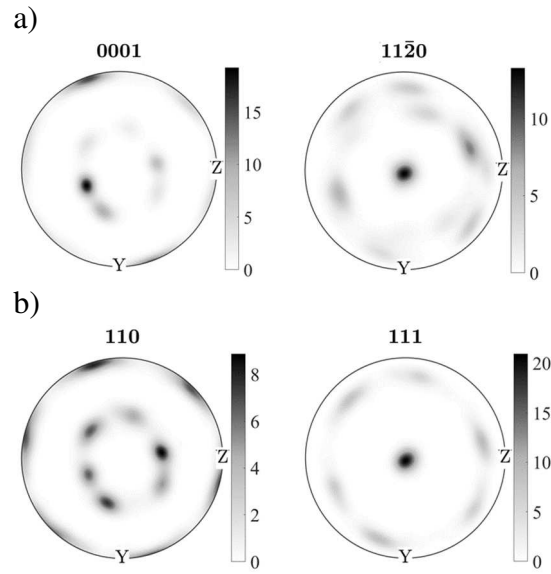
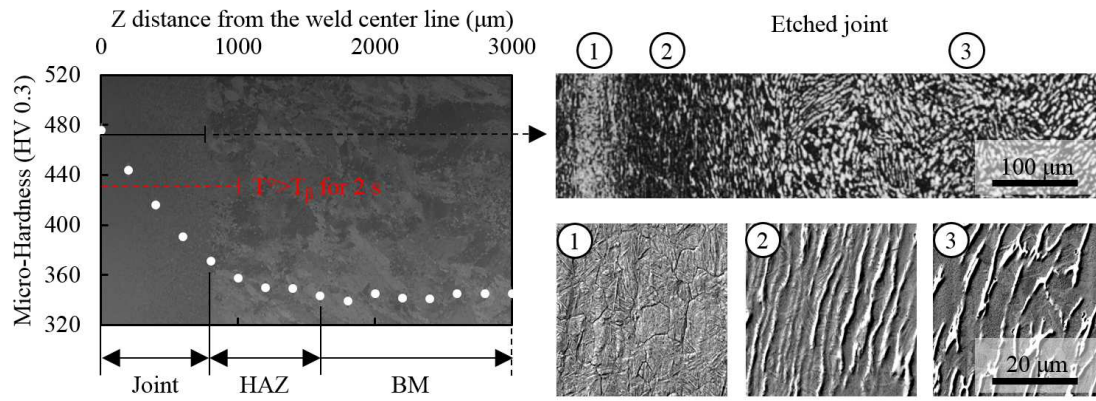


Figure 24 : a)  $0001$  and  $11\bar{2}0$  pole figures of the  $\alpha$  phase b)  $110$  and  $111$  pole figures of the  $\beta$  phase in the acicular central band after PWHT showing weakened  $\{0001\}\langle 11\bar{2}0\rangle$  and  $\{110\}\langle 111\rangle$  textures compared to the as-welded WL.



*Graphical abstract:* Multi-scale and multi-technic analysis of a linear friction welded near- $\alpha$  Ti6242 joint revealing a significant microstructural refinement and a consistent hardening due to extreme thermo-mechanical processing transforming the as-received fully-equiaxed microstructure into: ① martensitic laths precipitating within recrystallized prior- $\beta$  grains; ②-③ plastically deformed and fragmented  $\alpha$  nodules.